Neutral pion production in the reactions $^{16}O+^{27}Al$, ^{58}Ni, ^{208}Pb at 95 MeV/u.

Christian Moisan

Department of physics
McGill University, Montréal

A thesis submitted to the Faculty
of Graduate Studies and Research
in partial fulfillment of the requirements
for the Degree of Master of Science

January 4, 1990

Abstract

The inclusive production of neutral pions has been measured in reactions of 95 MeV/nucleon $^{16}O + ^{27}Al$, ^{58}Ni, ^{208}Pb, using a setup of 8 lead-glass Cherenkov counter telescopes to detect in coincidence the two photons resulting from pion decays. The differential distributions of interest: $d\sigma/dT_\pi$, $d\sigma/d\Omega$, $d\sigma/dy$ and $d\sigma/dp_t$ are obtained from the experimental invariant cross section of the pions. The transverse momentum, kinetic energy, and angular distributions, are discussed in the framework of the moving thermal source model. The shape of $d\sigma/dp_t$ and $d\sigma/dT_\pi$ is reproduced by a single source having a temperature close to 20 MeV and moving with a velocity between that of the nucleus-nucleus and the nucleon-nucleon center of mass rest frames. Relevant signatures of the energy and angular dependences of pion reabsorption have been extracted from the data. The deviations of the energy distributions from the thermal model predictions are consistent with the deduced behavior of reabsorption. It is also shown that the absorption can explain the evolution of the anisotropy of the angular distributions with the target mass.

Résumé

La production inclusive de pions neutres a été mesurée pour les réactions $^{16}O+^{27}Al$, ^{58}Ni, ^{208}Pb à 95 MeV/nucléon. La mesure fut effectuée à l'aide d'un montage de 8 télescopes composés de compteurs Cherenkov du type verre à plomb, permettant la détection en coïncidence des deux photons de désintégration du pion. La section efficace invariante expérimentale permet d'obtenir les distributions différentielles d'intérêt, soit: $d\sigma/dT_\pi$, $d\sigma/d\Omega$, $d\sigma/dy$ et $d\sigma/dp_t$. Les spectres en énergie et en moment transverse de même que les distributions angulaires furent étudiés en supposant que les pions originent d'une source thermique en mouvement. La forme de $d\sigma/dp_t$ et $d\sigma/dT_\pi$ est reproduite par une source unique ayant une température près de 20 MeV et se déplaçant avec une vitesse intermédiaire à celle du centre de masse noyau-noyau et du centre de masse nucléon-nucléon. Les résultats expérimentaux ont permis la mise en évidence des dépendances énergétiques et angulaires de la réabsorption des pions. Les écarts entre les distributions en énergie mesurées et celles prédites par le modèle thermique sont en accord avec le comportement déduit pour l'absorption. L'évolution de l'anisotropie des distributions angulaires avec la masse de la cible est elle aussi expliquée par la réabsorption des pions.

Acknowledgements

I am indebted to the following people for investing time with me in knowledgeable discussions:

At SUNY, Stony Brook; Dr Johanna Stachel, Dr Peter Braun-Munzinger and Dr Gerhard Ingold.
At McGill University; Dr Charles Gale, Dr Nicholas de Takacsy and Dr Subal Das Gupta.
Au CEN de Saclay; Dr Nicolas Alamanos et Dr Jean Julien.
At Michigan State University; Dr Georges F. Bertsch.

I also want to thank all those who took an active part in the realization of this experiment at GANIL, in June 88.

Catherine May Moroney's careful reading of the manuscript is worth a frank "Thanks a lot!".

This work would not have been possible without the financial support provided by the Natural Sciences and Engineering Research Council of Canada to the Foster Radiation Laboratory and to me personally via the "1967 Science and Engineering Scholarship", which is fully appreciated.

I kept the final word for my supervisor, Dr Jean Barrette. All along these two years spent at McGill, his continuous encouragements and constructive criticism have been great sources of motivation and achievement. No wonder, working with him has been quite instructive.

Christian Moisan

Contents

Figures

Tables

CHAPTER 1

INTRODUCTION

1.1 On Subthreshold Pion Production.

Linked to the search for the nuclear equation of state, the study of the dynamical evolution of heavy ion reactions has been an extensive field of research for the last 15 years. Nucleus-nucleus collisions at beam energies well above the Coulomb barrier, were soon identified as a good way of learning about highly excited nuclear matter. An essential requirement for the formation of such a system far from ground state equilibrium, is the transformation of a sizeable amount of the energy provided by the relative motion of the colliding nuclei. In the study of the cooperative mechanisms involved in the evolution of the hot internuclear zone, nonnucleonic probes such as mesons then attracted much attention. In contrast with nucleons, whose distribution shows strong projectile and target-like components, energetic mesons are likely to be produced by the participant fragments alone [Na81]. In addition, neutral mesons offer the advantage that they are not kinematically affected by Coulomb interactions with the remnants of the reaction.

Pions have no *a priori* existence in the nucleus. Their production in heavy ion collisions therefore requires that an energy of at least $m_\pi c^2$=135 MeV is made available in the center of mass frame at one stage of the reaction. Furthermore, this energy must be released by the system via one single channel, namely the creation of a π^0. If one considers the encounter between two free nucleons in a fixed target experiment, the creation of a neutral pion will be possible only if the laboratory energy of the incoming nucleon exceeds 280 MeV. When the reaction occurs between two nuclei, the same threshold applies for the total available energy in the center of mass. The situation is nevertheless very different. Now, all participant nucleons can share a

slight part of the energy necessary to create a particle. Therefore, in heavy ion reactions, neutral pions can be produced at beam energies much lower than the so called nucleon-nucleon threshold. The extreme situation implies the formation of a compound nucleus releasing all of its excitation energy into the creation of a pion. Using nonrelativistic kinematics and neglecting binding energy effects in the excited compound nucleus, the absolute laboratory threshold for this reaction $[A_p+A_t \rightarrow (A_p+A_t)+\pi^0]$ would be given by:

$$T_{th} = \frac{m_\pi c^2}{A_p}\left[\frac{(A_p + A_t)m_n c^2 + m_\pi c^2}{A_t m_n c^2 + m_\pi c^2}\right] \qquad (1.1)$$

For $^{16}O+^{16}O$, this amounts to 17 MeV/u. The closer the beam energy to the absolute threshold, the larger will be the number of nucleons from the projectile and the target acting coherently in the pion production mechanism. The study of neutral pion production below the nucleon-nucleon threshold is therefore seen as a unique tool to probe the importance of the cooperative mechanisms involved in nuclear reactions.

Many measurements of the inclusive neutral pion yield at beam energies ranging from 25 MeV/u to 85 MeV/u have been performed through the 80's. The following important results arose from these experiments. [Jo82, He84, Br84a, No84, St86, Yo86, Ju88a]

1: The total pion yield varies over several orders of magnitude within the beam energy range mentioned above. It can be as low as 1.28±0.27 nb for $^{16}O+^{27}Al$ at 25 MeV/u [Yo86], and climbs up to 174±21 μb for $^{12}C+^{238}U$ at 84 MeV/u [No84]. The experimental dependence of the production cross section upon the beam energy and its comparison against certain models that will be discussed later, is shown in Figure 1 (left).

2: The production cross section has a power law dependence upon the projectile and target masses. It is generally expressed as $\sigma\alpha(A_pA_t)^n$, where n is close to 2/3 [Br84a, No84]. However, the cross section levels

off slightly from this parametrization for heavy targets. This effect can be seen on the right hand side of Figure 1, where the target mass dependence of the total cross section is presented for various beam energies.

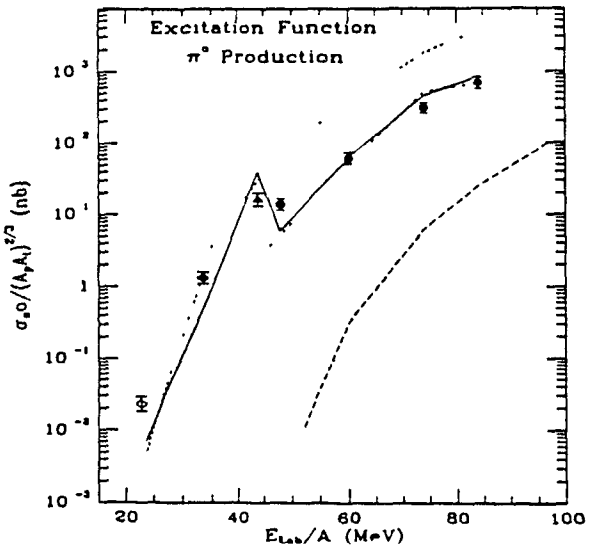

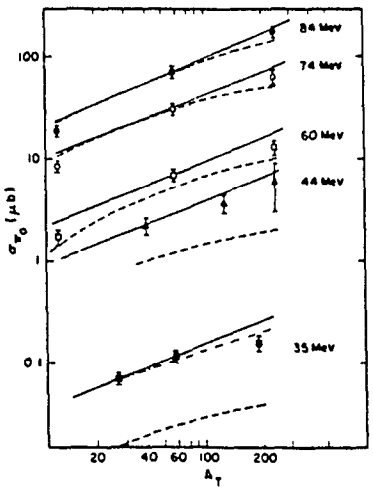

Fig. 1 (left) Comparison of the measured energy dependence of neutral pion production cross section with various model predictions. Long dashes [Gu84]; dashed-dotted line [At85]; solid line [Pr86]; short dashes [Sh84b]. The figure is borrowed from the reference [Br87]. (right) Mass dependence of the total cross section for different projectile energies. The respective projectiles were ^{14}N (35 MeV/u) [St86]; ^{40}Ar (44 MeV/u) [He84]; ^{12}C (60, 74, 84 MeV/u) [No84] The solid line corresponds to $\sigma\alpha A_t^{2/3}$, the dashed-dotted line to $\sigma\alpha(A_t^{2/3}A_p^{1/3}+A_t^{1/3}A_p^{2/3})$. The figure is after the work of reference [St86].

3: The kinetic energy distributions are typically exponential. Using the ansatz $d\sigma/dT_\pi \alpha \exp(-T_\pi/E_0)$, the inverse slope parameter E_0, equals 22±2 MeV below E_{lab}/A=60 MeV/u, regardless of the beam energy. As is seen in Figure 2, values slightly higher than E_0=22 MeV are reported at E_{lab}/A=74 MeV/u (E_0=25 MeV) and E_{lab}/A=84 MeV/u (E_0=28 MeV) [No84].

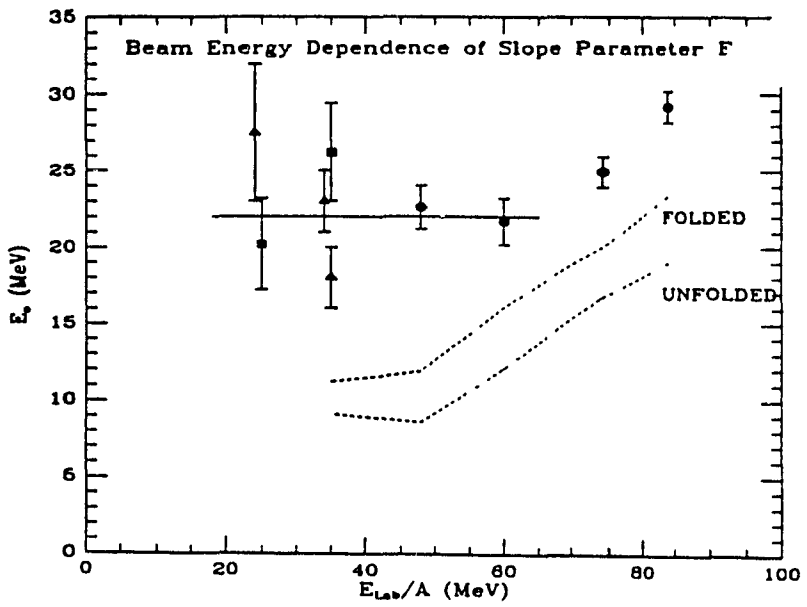

Fig. 2 Beam energy dependence of slope parameters deduced from pion kinetic energy distributions. Full circles: $^{12}C+^{12}C$ [No84]; full triangles: $^{16}O(^{14}N)+^{58}Ni$ [Br84a, St86]; full squares: $^{16}O(^{14}N)+^{27}Al$ [Br84a, St86]; open triangles: $^{14}N+W$ [Br84a, St86]. The dashed lines are predictions of Prakash et al. [Pr86] with and without taking into account the experimental resolution. The figure is borrowed from reference [Br87].

4: The angular distributions are anisotropic with a minimum at 90° in the center of mass frame of symmetric colliding systems such as $^{12}C+^{12}C$. As shown in Figure 3, this anisotropy is also found to increase with the kinetic energy of the pions.

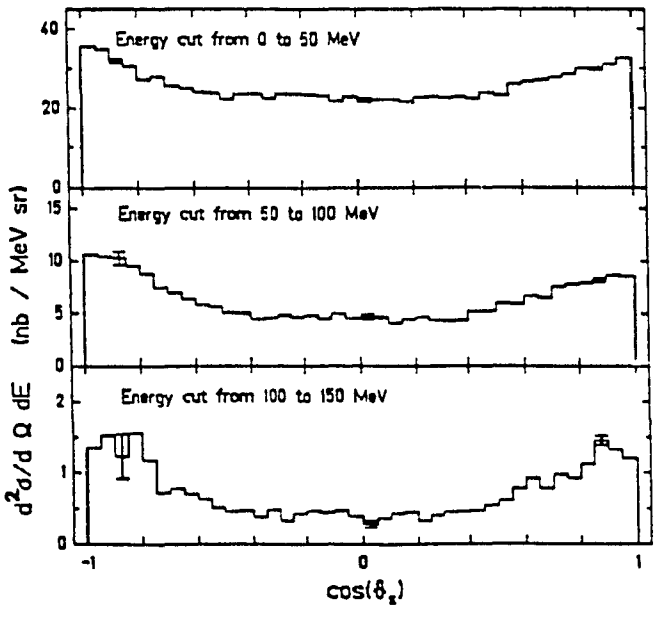

Fig. 3 Angular dependence of the neutral pion production cross section from $^{12}C+^{12}C$ at 84 MeV/u [No84]. The cross section is integrated over three energy ranges in the nucleus-nucleus center of mass. The figure is from reference [Gr85].

5: Finally, for asymmetric colliding systems, the invariant cross sections are consistent with pions emerging from a source moving with a velocity between that of the nucleus-nucleus β_{CM}, and the nucleon-nucleon β_{NN}, center of mass rest frames. This suggests that several nucleons from both, the projectile and the target, participate in the production mechanism. Note that an apparent source velocity of β_{CM} would be consistent with pions originating from a compound nucleus, while a production dominated by first chance $NN \rightarrow NN\pi$ collisions would result in an apparent source moving with β_{NN}.

Numerous theoretical approaches have been suggested in attempt to reproduce the main features of pion production far below the nucleon-nucleon threshold. Only a survey of those models based on the nucleon-nucleon collision mechanism or related to the thermal source prescription will be presented here. A complete review of all models available in the literature before 1987 can be found in the reference [Br87].

A dynamical investigation originally proposed by McMillan & Teller in 1947 [Mc47] to account for the first observed pions produced below the nucleon-nucleon threshold, has been reintroduced by Bertsch [Be77] in the context of heavy ion collisions. In this first "contemporary" model, subthreshold pion production occurs from first chance Fermi boosted nucleon-nucleon collisions, $NN \rightarrow NN\pi$. The pionic production cross section is obtained using a pure Fermi gas model to parameterize the momentum distribution of the target and projectile nucleons The predicted pion yield then results from the folding of the momentum distribution with the intrinsic cross section $\sigma^{free}[NN \rightarrow NN\pi]$. In this model, a lower limit on the pion production appears when the relative momentum of the colliding nucleons is equal to 1.18 of the Fermi momentum. Below this value, which corresponds to $E_{lab}/A \cong 54$ MeV/u, the predicted cross section falls off steeply and fails to reproduce the experimental data.

Guet & Prakash tried to avoid the inconsistencies implied in Bertsch's naive picture, which could deal neither with the Pauli exclusion principle nor with bound nucleons orbiting on their

respective shell. In their model [Gu84], they overcame possible effects due to Pauli blocking by considering only those single nucleon-nucleon collisions where an incoming nucleon, with off-shell energy-momentum, scatters to the inelastic channel in which a π^0 and two nucleons are left free. Furthermore, the momentum distribution of a harmonic oscillator was taken as an approximation to the shell model. This mechanism results in large cross sections above 100 MeV/u. Nevertheless, it still underpredicts considerably the data below E_{lab}/A=50 MeV/u even if strong mean field effects are considered by introducing the attractive ion potential.

It is clear that an important feature is absent of the two previous Fermi gas models. The perturbation of the nucleon wave functions during the collision ought to be included in any consistent dynamical approach. In a second generation of models based on single nucleon-nucleon collisions, more attention has therefore been paid to the time evolution of the reaction and the influence of the nuclear mean field. Blann [Bl85] obtained a time dependent momentum distribution for the colliding nucleons using the Boltzmann master equation. Aichelin [Ai85] on the other hand, used the Boltzmann-Uehling-Uhlenbeck method, which consistently incorporates the nuclear mean field, two-body kinematics and Pauli blocking effects to describe the time dependence of the collision dynamics. Tohyama et al., [To84, To85] accounted for the temporal evolution of the nuclear mean field in the framework of the Time-Dependent-Hartree-Fock theory. In this model, Fermi motion, Pauli Blocking and the deformation of the momentum distribution are all implicitly built in. Recently, Cassing [Ca88], also studied the time dependence of the mean field due to the relative motion of the reaction partners and the nucleon-nucleon collisions within a microscopic quantal phase space approach.

These sophisticated versions of the single nucleon-nucleon collision prescription all satisfactorily reproduce the beam energy dependence of subthreshold pion production. This would suggest that by properly describing the two-body dynamics and its influence on the mean field, one obtains a good description of the data with no special need for collective enhancements. However, these models say little about or even fail to reproduce several important features of the data.

For instance, the constant value $E_0 \cong 23$ MeV of the inverse slope parameter observed with decreasing beam energy is not reproduced by the single nucleon-nucleon collision mechanism. Blann [Bl85] is in fact the only one who reports kinetic energy spectra, and his inverse slope parameters are much higher than those measured in the beam energy range of 20 to 85 MeV/u. Also, the apparent source velocity resulting from individual nucleon-nucleon collisions within the first collision approximation are of half that of the beam. This is at variance with the velocity experimentally observed for asymmetric projectile-target systems.

The thermal model provides another tempting framework for the study of subthreshold pion production. Here, one assumes that collisions between nucleons quickly result in the formation of a "hot zone". The thermalization of the center of mass energy subsequently leads to the emission of pions, as a possible decay channel, whenever the excitation energy of the compressed zone exceeds $m_\pi c^2$.

Aichelin & Bertsch [Ai84a] first applied this idea. They considered that all target and projectile nucleons are involved in the formation of a compound nucleus. In their model, the excitation energy is given by the energy available in the center of mass and the mass excess of the colliding nuclei. The Weisskopf theory is then applied to statistically describe the decay of the excited system. The decay probabilities are calculated by summation of the nuclear level densities folded by the absorption (inverse) cross section for a given output channel. In this model, the cross section for the formation of a compound nucleus is the only free parameter that remains unknown and which must be adjusted to fit the data.

Because it required all nucleons to be part of a compound nucleus, the first thermal model of Aichelin & Bertsch was inconsistent with the observed rise of the pion production cross section with the target mass. Nevertheless, Aichelin [Ai84b] and Gale & Das Gupta [Ga84], succeeded in reproducing the energy dependence of the total pion production cross section within the thermal approach, assuming that only a subset of nucleons were part of the hot spot.

The description of a statistically decaying thermalized volume has been further generalized independently by Prakash et al. [Pr86] and Shyam & Knoll [Sh84a, Sh84b, Sh86]. In both descriptions, the local hot zone decay probability is given by the available phase space for many particle output channels. The invariant pion production cross section is described in terms of a formation cross section of the hot spot, and its overall decay probability obtained by adding all possible output channels. Prakash et al. used the fireball model to predict the formation cross section of the excited zone. On the other hand, Shyam & Knoll evaluated the latter for each impact parameter using cascade calculations. As indicated by the experimental invariant cross sections, both models have also assumed full stopping in the nucleon-nucleon center of mass, but not in the compound nucleus system. It is in the calculation of decay probabilities that these models have taken different avenues. In the model of Prakash et al., the Weisskopf theory was used only for two-body output channels, while Shyam & Knoll chose to count with equal probability all available phase space cells for multibody final states, including clusters of nucleons. The predictions of those two models are compared with the experimental data on Figure 1 (solid line [Pr86]; short dashes [Sh84b]). If the description of Shyam & Knoll generally overestimates the inclusive pion cross section, the model of Prakash et al. is very successful. It even reproduces the kink near 44 MeV/u, reflecting the deviation of the data from the simple $\sigma\alpha(A_pA_t)^{2/3}$ scaling law. Discrepancies however appear when the kinetic energy distributions predicted by these two models are set against the experimental ones. Both calculations lead to spectra that are steeper than the observed $d\sigma/dT_\pi$. At $E_{lab}/A=35$ MeV/u, they respectively predict inverse slopes of 11 and 6 MeV, while the experimental E_0 is close to 23 MeV [St86]. Besides, as a consequence of the thermal assumption, the predicted angular distribution of the pions is isotropic in the center of mass of the hot zone; this clearly prevents these models from accounting for the rather high anisotropy observed in $d\sigma/d\Omega$

1.2 The Experiment.

The fact that models based on the nucleon-nucleon collision mechanism or on the thermal source prescription can account for the beam energy dependence of the subthreshold pion production but fail to predict the general features of the kinetic energy and angular distributions makes a final theoretical discussion difficult. In an attempt to isolate the cooperative component involved in the subthreshold pion yield, much attention has been paid to measurements very close to the absolute laboratory cut off [He84, St86, Yo86, Ju88a]. Because of the small production cross sections at these energies, the results, especially for $E_{lab} \leq 50$ MeV/u, have suffered from a poor statistics. This have caused the discussion of different models to be very difficult due to a lack of significant experimental signatures. Furthermore, very little is actually known, both theoretically and experimentally, on the eventual effects of the reabsorption of pions in the surrounding nuclear matter after their emission. What are the energy and angular dependences of pion reabsorption? Does absorption act at a perturbative level or completely bias the observed inclusive data? These are questions still waiting for better experimental informations. Especially, the effect of reabsorption on the primary pion distribution clearly deserves more attention if one hopes to comment on the validity of the models. Under these considerations, it appeared that an extensive study of neutral pion production close to 100 MeV/u was relevant Hence, using a dedicated setup, the inclusive production of neutral pions in reactions of 95 MeV/u $^{16}O+^{208}Pb,^{58}Ni,^{27}Al$ has been measured† at the two coupled isochronous cyclotrons GANIL (Caen, France). At this energy, enough statistics was expected to find signatures helpful in understanding the mechanisms involved in the subthreshold production of pions. One also aimed to isolate the behavior of pion reabsorption and to discuss how it affects the primary pion distribution.

† A complete list of the persons involved in this experiment is given in the appendix.

CHAPTER 2

EXPERIMENTAL PROCEDURE

2.1 Detection of Neutral Pions.

Neutral pions have a total lifetime of 8.7×10^{-17} seconds and decay through their dominant channel $\pi^0 \rightarrow \gamma\gamma$ with a branching ratio of 98.8%. Those emitted with a kinetic energy below 200 MeV will therefore decay while they are still in the target material Under such considerations, the inclusive study of π^0 production is achieved by detecting two coincident photons of energy between 20 and 200 MeV, depending on the detailed kinematics of the pion decay.

The active detectors of the π^0 spectrometer used for the present experiment were total absorption lead-glass Cherenkov counters. Their effectiveness in detecting hard photons produced in neutral pion decays has been long established by many groups [Be74, Ba81, Mi86]. In these Cherenkov counters, the detection mechanism is governed by the rules of electromagnetic calorimetry. When a photon passes through the detector, a finite probability exists that an initial pair conversion $\gamma \rightarrow e^+e^-$, will trigger a secondary shower of photons and leptons $e^{\pm}$. The Cherenkov light generated by this cascade along its path then provides a signal proportional to the total energy of the incoming photon

2.2 *Schematic Layout.*

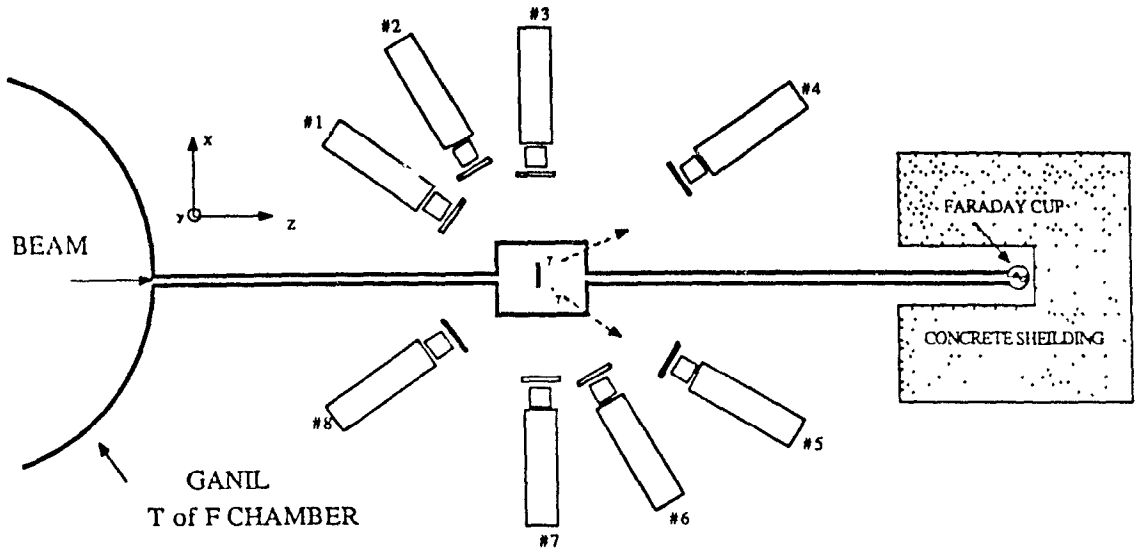

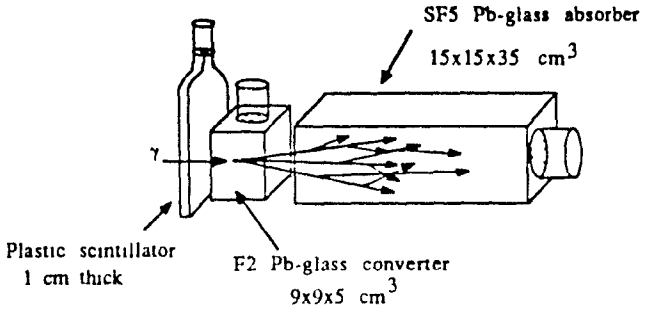

Fig. 4 (top) Schematic layout of the neutral pion spectrometer used in the present experiment. (bottom) A view of a scintillator-converter-absorber telescope unit used for energetic photon detection.

A schematic layout of the detection setup is shown in Figure 4. The π^0 spectrometer was composed of 8 telescopes oriented toward the target in a plane containing the beam axis. The entire detection system was mounted downstream from the time of flight chamber in cave D1 of the GANIL experimental hall. As displayed on the figure, each module consisted of an active converter of F2 Pb-glass [radiation length X_0=3.1 cm, area=9x9 cm^2, thickness=5 cm], backed by a SF5 Pb-glass absorber [radiation length X_0=2.4 cm area=15x15 cm^2, length=35 cm]. The thickness of the converter was such that incoming photons in the energy range considered here had a maximum probability to generate

an electromagnetic shower with signals above threshold in both Pb-glass elements of the telescope. In addition, the lateral and longitudinal dimensions of the absorber were picked to ensure that showers of photons up to 300 MeV would be confined in all directions. The Cherenkov light produced in the converter was collected by a fast rise time photomultiplier. A long rise time phototube, 7.5 cm in diameter, was glued directly on the back of the absorber to detect most of the Cherenkov signal generated by the incoming photon. In order to avoid triggering on charged particles, the converter was preceded by a 1 cm thick plastic paddle used as a veto in the electronic logic flow. Since they had a radiation length of 48 centimeters, these plastic scintillators cut less than 2% of the good two-fold coincidence events.

In Table 2.1, the polar coordinates [R, Θ, Φ] of each telescope are provided as measured from the target to the center of each converter. The energy thresholds applied on the converter and absorber are also given for later use.

Table 2.1: *Experimental specifications of the detectors*

#ID	*R(cm)*	Θ *(deg)*	Φ *(deg)*	Thr_C *(MeV)*	Thr_A *(MeV)*
1	35.0	148	0	6.5	11.5
2	35.0	120	0	6.5	12.0
3	35.0	90	0	6.5	14.0
4	60.0	38	0	5.5	12.5
5	60.0	32	180	5.0	12.5
6	40.0	60	180	4.5	13.0
7	35.0	90	180	3.0	10.0
8	35.5	142	180	6.0	10.5

In this configuration, a solid angle of 3.4% of 4π was covered in the laboratory by the spectrometer. The specific choice of distances resulted from a compromise between an optimum angular resolution on the emission direction of the detected photons and a high geometrical detection efficiency. The distribution of axial angles Θ_i, was chosen not to be uniform so that the opening angles ϕ_{ij}, characterizing the 28 possible telescope pairs were almost evenly spread between 0^o and 180^o. As will be shown in the next chapter, the π^0 kinematics is closely related to the opening angle $\phi_{\gamma 1 \gamma 2}$ between the decay photons.

Consequently, the ϕ_{ij} distribution of our spectrometer is directly transposed in the overall shape of its geometrical efficiency to the detection of $\pi^0 \rightarrow \gamma\gamma$ decays.

The thicknesses of the ^{208}Pb, ^{58}Ni and ^{27}Al targets were 125, 180 and 135 mg/cm^2 respectively; these resulted in energy losses inferior to 4% of the total energy for the 95 MeV/u beam of ^{16}O. With average beam intensities of 15 nAmps, runs of about 12 hours were sufficient to obtain for each target a statistics of about 10^4 good $\pi^0 \rightarrow \gamma\gamma$ events. These runs were twinned with hard photon measurements on the same targets ($M \geq 1$ Trigger). Finally, as part of the calibration [see section 3.1] and in order to follow the gain drift of the detectors, acquisition runs of 1 hour on cosmic muons have preceded and terminated the study of each target.

2.3 *Electronics.*

A layout of the aquisition setup used for the neutral pion detection is presented in Figure 5. The detailed electronic diagram of only one telescope unit is displayed.

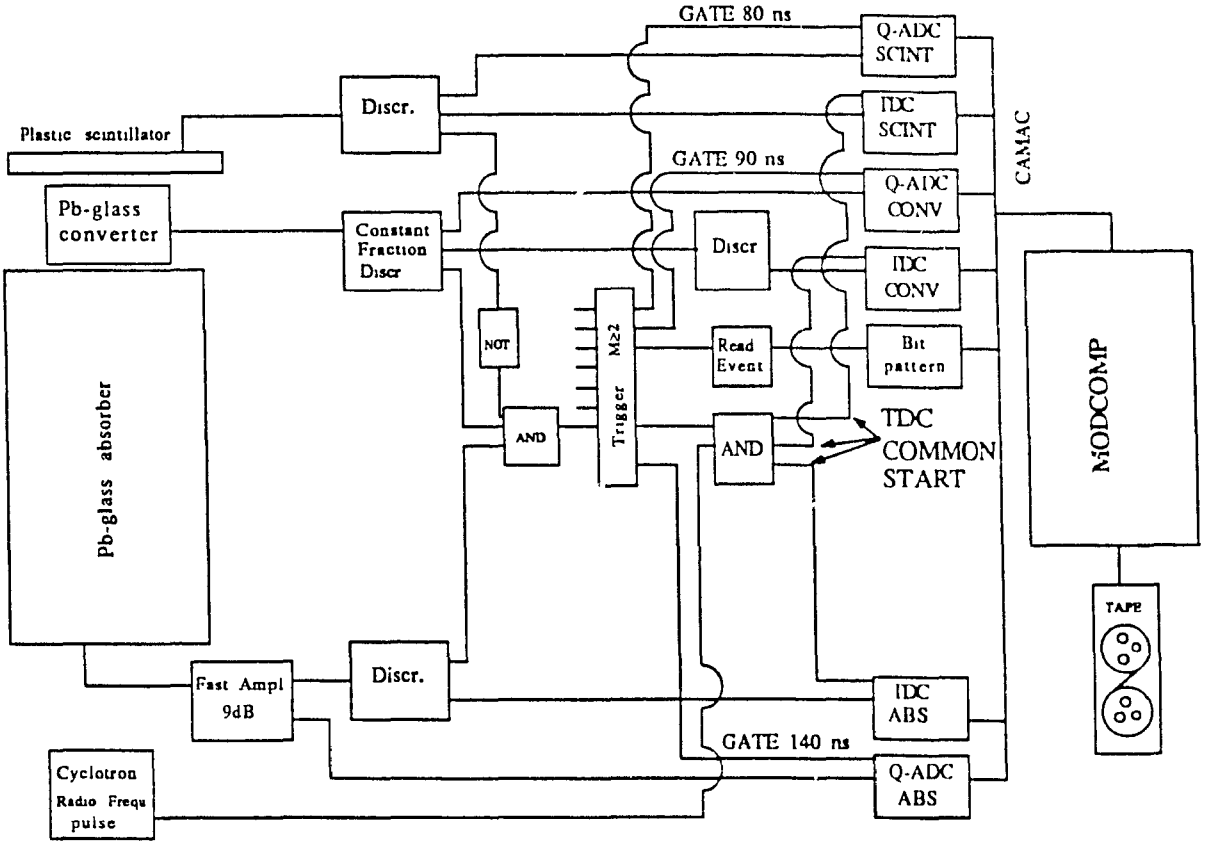

Fig. 5 Layout of the electronic setup.

A single photon event was identified by coincident pulses above the respective thresholds of the converter and the absorber. As mentioned, signals from the many charged particles produced by heavy ion collisions at these energies, were rejected by a veto applied on the coincidence unit using the plastic scintillators output. A good $\pi^0 \rightarrow \gamma\gamma$ event was triggered by requiring that at least two telescopes fired. For these two-folds and higher multiplicity events, a READ command was issued to the CAMAC controller, and subsequently, the energy and time signals from the scintillator, converter and absorber of each telescope involved in the event were registered on magnetic tape The M≥2 trigger box was used to generate the integration gates for the charge sensitive analog to digital converters Q-ADC's. A bit pattern word

containing the identification number of all firing telescopes was also generated from this module.

The time-to-digital converter (TDC) common START was provided by a coincidence between the trigger box and the cyclotron radio frequency pulse. The TDC STOP signals for the absorbers and scintillators were generated from quadratic leading edge discriminators. In order to achieve a maximum separation of the important neutron background, special care was paid to the timing of the converters by using constant fraction discriminators. With an appropriate walk adjustment, the time interval between the cyclotron radio frequency pulse and the converter STOP signal had an average resolution of 1.5 nsec. As shown in Figure 6, this allowed a good separation between the pion decay photons and most of the neutron background in the converter TDC spectra.

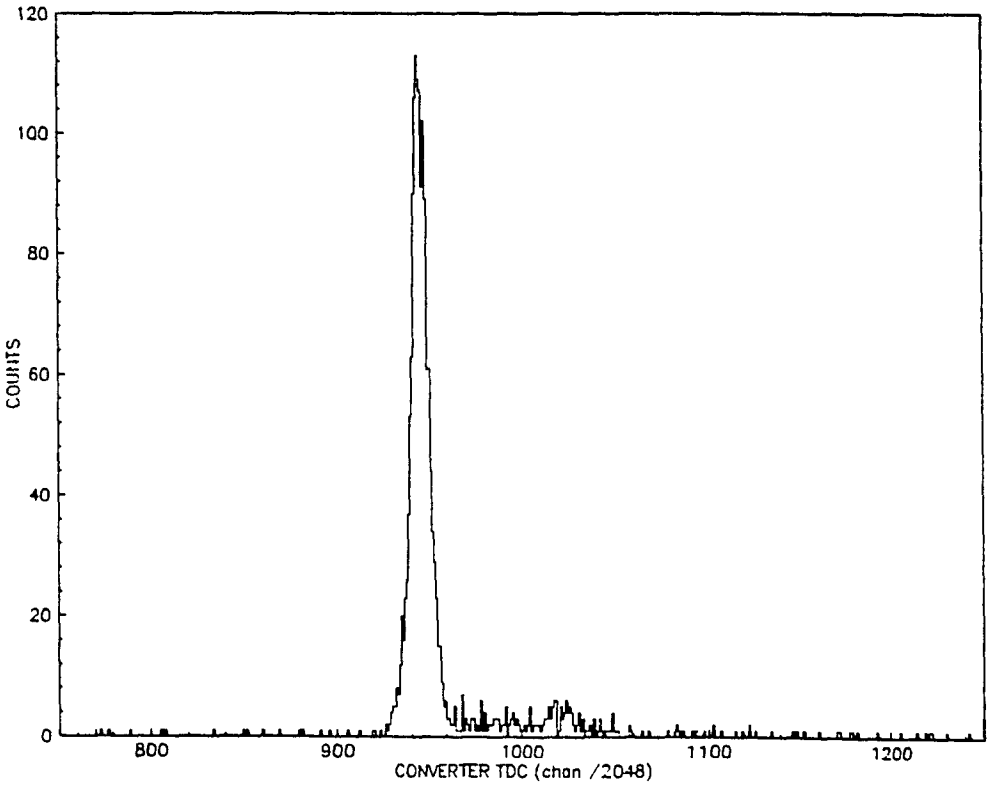

Fig. 6 Typical converter TDC spectrum. The shoulder which follows the strong photon peak is mostly due to neutrons.

CHAPTER 3

DATA ANALYSIS

3.1 Energy Calibration.

As was mentioned in the introduction of the previous chapter, the total Cherenkov light pulse emitted by an electromagnetic shower propagating in a Pb-glass detector is proportional to the energy of the detected photon. This key property is intimately related to the energy degradation mechanisms at work in the detector material. Fundamentally, the dissipation of the initial energy through a cascade of particles is governed by the rules of statistics, and the average number of secondaries contained in the cascade is proportional to the total energy E_t of the incoming particle [Fa82, Pe87a]. In the case of an electromagnetic shower, this statistical behavior is dominated by pair creation $\gamma \rightarrow e^+e^-$ and bremsstrahlung radiation $e^{\pm} \rightarrow \gamma e^{\pm}$, which are the two main energy dissipation channels for photons and energetic electrons. As usual, in a Cherenkov counter the detection is experimentally achieved by collecting a signal resulting from a stimulation of the detector material. In a dense block of lead-loaded glass, this signal arises from the fraction of energy lost through the excitation of density fluctuations by relativistic $e^{\pm}$; fluctuations which in turn translate into Cherenkov radiation [Ja75]. The total measurable light pulse results from the sum of the Cherenkov signals contributed by each $e^{\pm}$ track segments present in the cascade. Because the number of these is proportional to E_t, one obtains a linear relationship between the collected output and the detected particle energy.

Accordingly, the calibration function used in the present analysis, linearly links the detected photon energy and the Cherenkov light pulses encoded by the converter and absorber Q-ADC's. The total energy E_γ of a photon hitting a given telescope i, is assumed to be given by the following function:

$$E_\gamma\,(\mathrm{MeV}) = M_i\left[\frac{(\mathrm{QADC}_{Ai}-P_{Ai})}{\mu_{Ai}} + R\,\frac{(\mathrm{QADC}_{Ci}-P_{Ci})}{\mu_{Ci}}\right] \qquad (3.1)$$

The constants P_{Ai} and P_{Ci} are the respective absorber and converter Q-ADC's pedestal offsets, and were simply obtained by triggering the acquisition with a pulser. The constants μ_{Ai} and μ_{Ci} were introduced in the calibration in order to normalize the relative gain of each Pb-glass detector and follow their drift. They are derived from the centroid of the cosmic muon spectrum measured in each absorber and converter during the experiment. A simple way of matching the gains was to choose values of μ_{Ai} and μ_{Ci} such that the centroid [minus the pedestal] of the cosmic muon spectrum measured in each detector was centered at a constant and arbitrary Q-ADC channel. One could also correct for the gain drift of the converters by using the centroids obtained for the cosmic run which was the closest to the π^0 measurement of each target to calculate μ_{Ai} and μ_{Ci}.

A typical converter Q-ADC cosmic-ray spectrum is shown in Figure 7a.

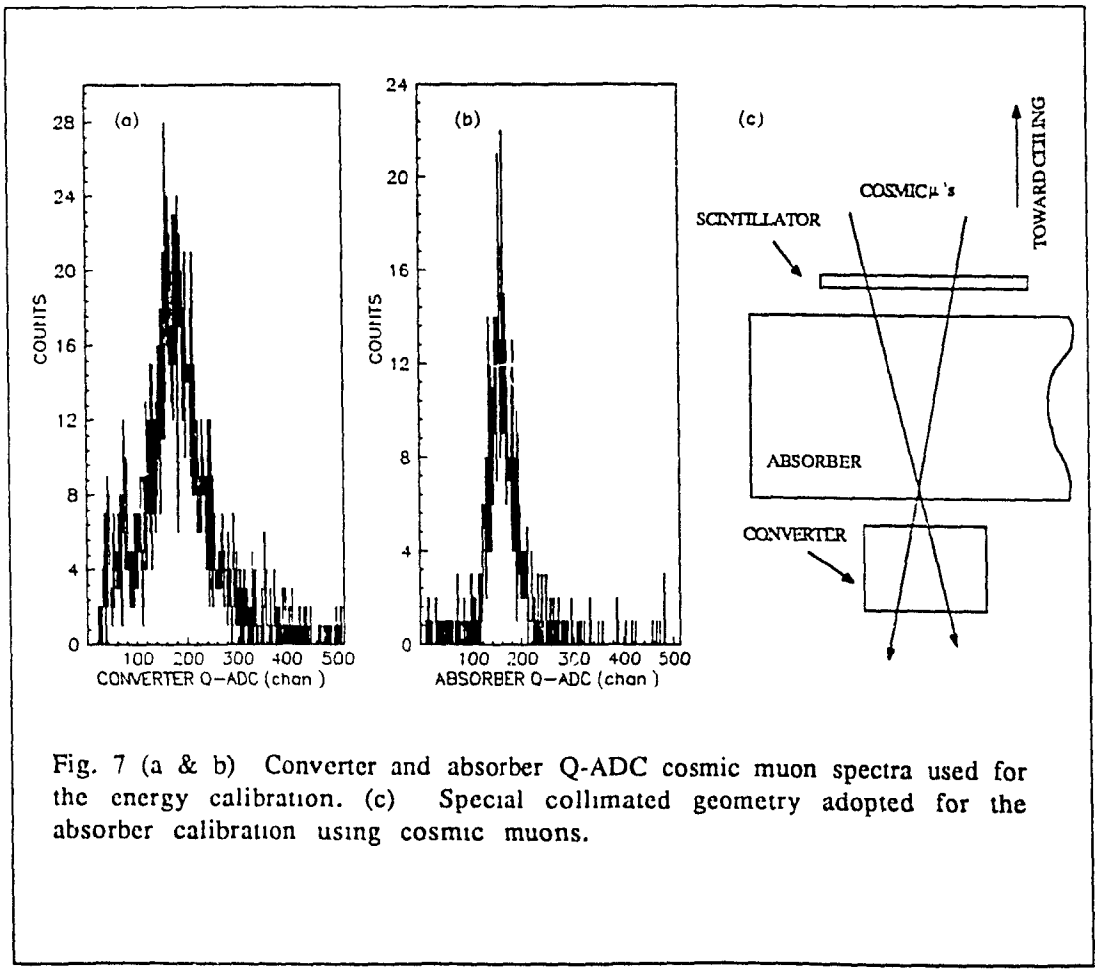

Fig. 7 (a & b) Converter and absorber Q-ADC cosmic muon spectra used for the energy calibration. (c) Special collimated geometry adopted for the absorber calibration using cosmic muons.

A triple coincidence scintillator-converter-absorber has been used to trigger a good cosmic event. For this measurement, the converters were left in the horizontal telescopic geometry of the π^0 spectrometer. Similar spectra were measured every 24 hours for all the converters in order to monitor their stability. For the absorbers, an horizontal telescopic configuration could not provide a sufficient collimation of the cosmic muon trajectories and typically resulted in asymmetric tailing distributions. For this reason, the characteristic energy loss distribution of cosmic muons was measured for the absorbers at the very beginning of the experiment using a more appropriate geometry (see the right hand side of Figure 7). An absorber Q-ADC spectrum obtained in this configuration is shown in Figure 7b. To test the stability of all absorbers, the same procedure was repeated at the end of the experiment. This last verification confirmed that the centroids of the cosmic muon spectra have not shifted by more than ±3% of their initial value.

Once all absorbers and converters gains have been separately matched, the relative absorber to converter calibration was established by chosing the constant R. In the present calibration, the exact value of R was chosen so that the ratio of the converter and absorber contributions to the total energy of an average cosmic muon equals 32.5% for any telescope. This figure was obtained from a systematic study of the present Pb-glass detectors at the 600 MeV Saclay electron LINAC using tagged photons of 20 to 100 MeV [Ju88b]. It is also in good agreement with previous findings reported by Stachel et al. [St86] under similar conditions. Note that μ_{A_i}, μ_{C_i} and R only provide the relative energy calibration. However, with these constants as defined, the calibration function is constrained to yield the same average energy loss for cosmic muons in all the absorbers or converters separately. Furthermore, the converter to absorber energy loss ratio is unique and constant for all the telescopes, as it must be, since for minimum ionizing particles, such as cosmic muons, the energy loss is independent of the particle energy and is only determined by the thickness of the detectors.

The absolute energy scale of the calibration is provided for each telescope by the constant M_i. These have been obtained by fixing the

dominant π^0 peak present in the experimental invariant mass distribution at a value of $m_{inv}c^2$=135 MeV. Using conservation of the total 4-momentum in the $\pi^0 \rightarrow \gamma\gamma$ decay, it is easily shown that the neutral pion's invariant mass is given by:

$$m_\pi c^2 = 2\sqrt{E_{\gamma i} E_{\gamma j}}\ \sin(\phi_{ij}/2) \qquad (3.2)$$

where $E_{\gamma i}$ and $E_{\gamma j}$ are the photon laboratory energies measured in the coinciding telescopes i and j that are separated by an opening angle ϕ_{ij}. In Figure 8, the invariant mass distribution obtained for the reaction $^{16}O + ^{208}Pb \rightarrow \pi^0 + X$ by considering any two-fold coincidence involving telescope #3 is displayed. After a few iterations over all possible telescope pairs, the calibration constant M_3 converged to a value that fixed the dominant π^0 peak at 135 MeV.

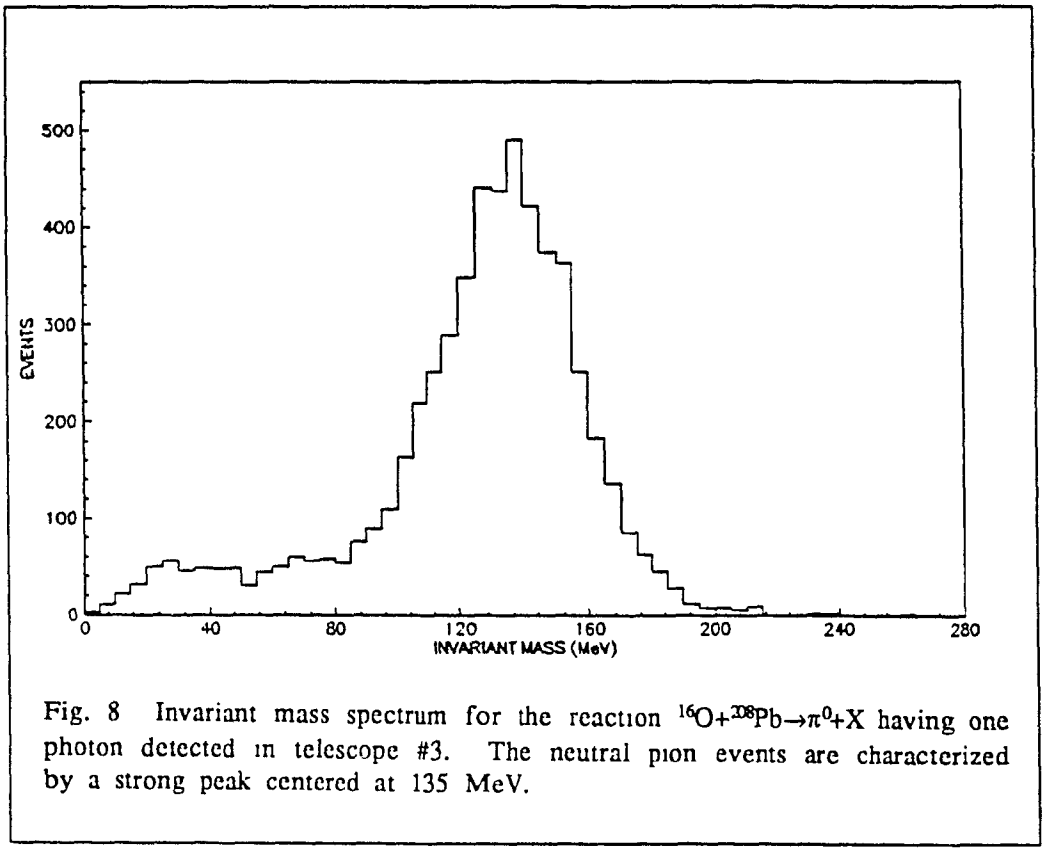

Fig. 8 Invariant mass spectrum for the reaction $^{16}O + ^{208}Pb \rightarrow \pi^0 + X$ having one photon detected in telescope #3. The neutral pion events are characterized by a strong peak centered at 135 MeV.

Considering similar distributions for each of the detectors, an average resolution [FWHM] of 39±3% is obtained for the neutral pion

peak of the invariant mass distribution. This value is mainly determined by the intrinsic energy resolution of the Pb-glass detectors [see section 3.4]. Also note that the value of the converter to absorber relative gain constant R, used in the present calibration, does not minimize the width of the invariant mass distribution.

Finally, for cosmic muons, with the energy calibration described above, an average energy loss of 140±7 MeV and 45±3 MeV is found in the absorbers and converters respectively. The errors quoted are representative of the variations in the constants M_i which provide the correct position of the invariant mass peak measured in each telescope during the whole experiment.

3.2 *Background Suppression.*

In this experiment, the major source of background is beam correlated. Nuclear deexcitation γ-rays are produced with an average multiplicity of 20 to 30 in intermediate energy nuclear reactions. Therefore, when considering a geometric cross-section of a few barns for the reaction between two heavy ions and a π^0 production at the level of 100 nano barns, one expects only 10^{-9} to 10^{-8} of the photon yield to come form $\pi^0 \rightarrow \gamma\gamma$ decays. With typical temperatures of 1 to 2 MeV, the nuclear deexcitation photon background is easily suppressed with the natural high energy threshold offered by Pb-glass Cherenkov counters. This is shown on Figure 9 for telescope #3 of the detection setup. As listed in Table 2.1, the discriminators were adjusted to provide average hardware thresholds of 5.5 and 12 MeV on the converters and absorbers respectively, this corresponding to a total energy threshold of 17.5 MeV on each single photon hit. The detection of nuclear deexcitation photons produced with an energy higher than the sum of the converter and absorber thresholds was also substantially cut down by the two-fold multiplicity trigger.

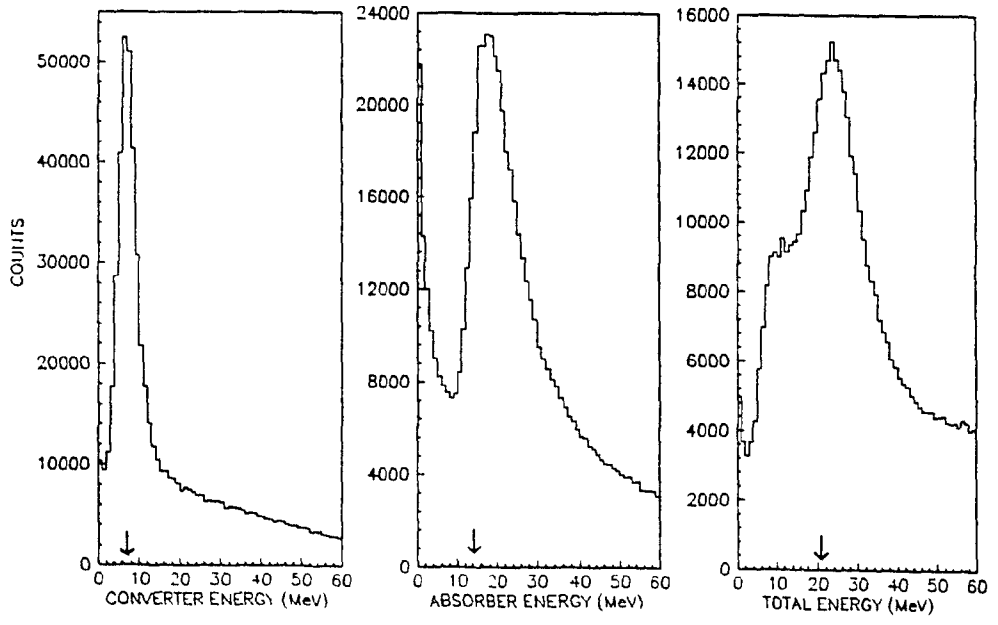

Fig. 9 Converter, absorber and total discriminator thresholds applied on the telescope #3 of the setup. The arrows correspond to the energy value at 3/4 of the peak maximum [also see table 2.1].

Contributions from slow Compton electrons, x-rays or photo-electrons are not expected to be an important source of background in presence of lead-glass detectors since they have a natural threshold of T_e>130 keV for electrons. High energy protons, abundantly produced at these energies in heavy-ion collisions, were also suppressed by a high energy threshold above 200 MeV in Pb-glass Cherenkov counters.

Fast neutrons, [T_n>50 MeV], form the main contribution to the overall background, especially in the forward detectors. The majority of these neutrons could be separated from the photon yield with an appropriate off-line gate on the converter TDC spectra. This is shown in Figure 10, which presents the TDC spectrum obtained in converter #7 of the π^0 spectrometer for the reaction $^{16}O+^{208}Pb\rightarrow\pi^0+X$. Most background events are resolved from the photon peak due to their large time of flight.

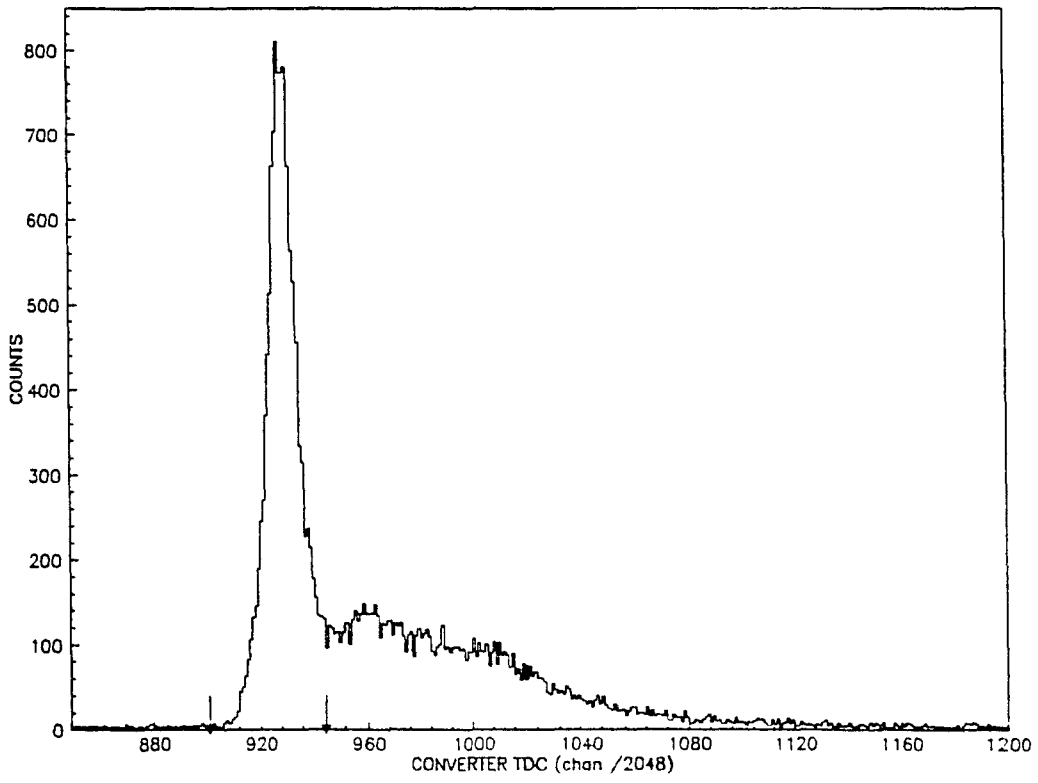

Fig. 10 Software gate (arrows) applied on the converter TDC spectrum of telescope #7. Most of the background events are characterized by a large time of flight and are easily resolved from the photon peak.

Among all of the two-fold events passing through the energy thresholds in both telescopes and satisfying the coincidence between their time gates, neutral pion decays could be identified by a peak at 135 MeV in the invariant mass distribution

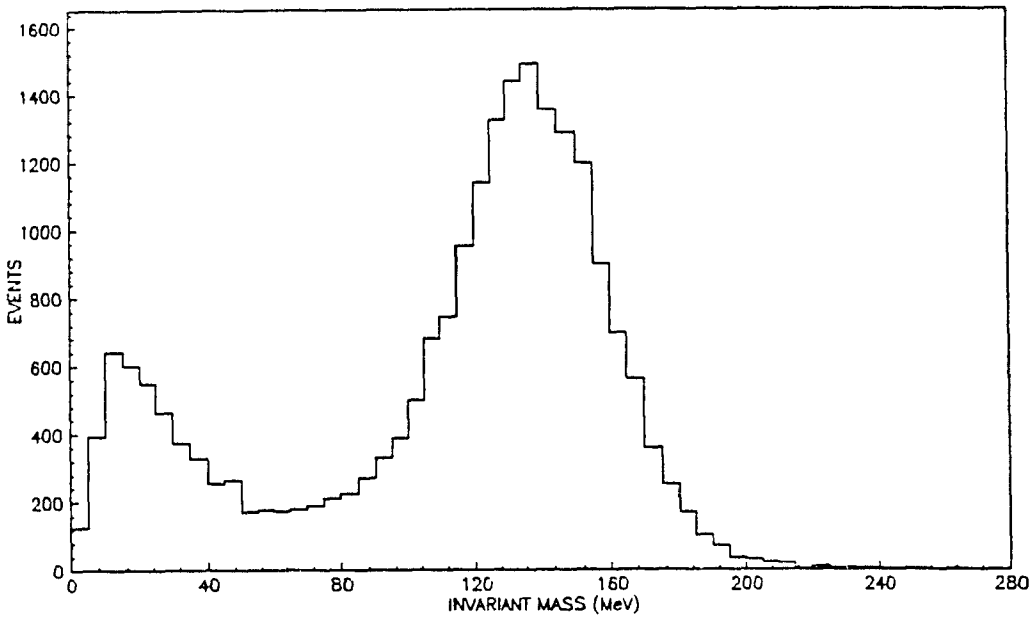

Fig. 11 Invariant mass spectrum obtained for the reaction $^{16}O+^{208}Pb\rightarrow\pi^0+X$ after a TDC gate has been applied on all converters. Remaining background events are grouped at low invariant mass.

Figure 11 clearly shows the presence of some remaining background counts grouped at low invariant mass; $m_{inv}c^2\leq 80$ MeV. The best part of it is due to high energy neutrons. A small fraction is also related to hadronic showers created in the concrete ceiling that are not vetoed by the plastic paddles. Both, the neutrons and the cosmic muons are characterized by rather low energy losses, and therefore lead to a low invariant mass value. This is shown in Figure 12a, where is presented a scatter plot of the detected energy E_γ and the resulting invariant mass $m_{inv}c^2$ for all two-fold coincidences obtained in the reaction $^{16}O+^{208}Pb\rightarrow\pi^0+X$ and involving the telescope #7.

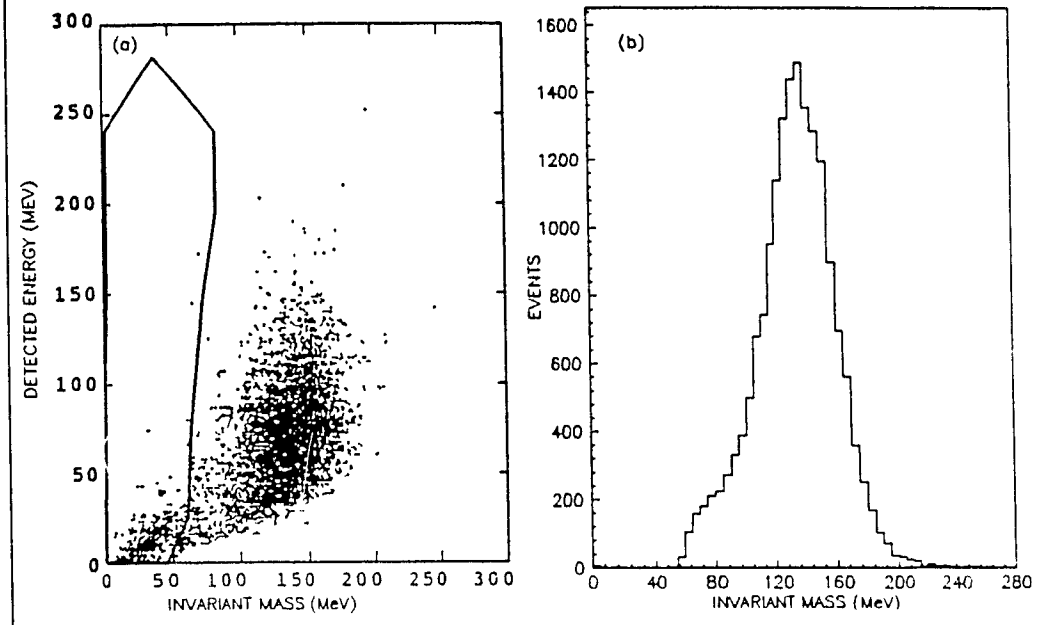

Fig. 12 (left) Scatter plot of the total energy and invariant mass of all events involving telescope #7 and a software gate applied on background counts. (right) Resulting total invariant mass spectrum for the reaction $^{16}O+^{208}Pb \rightarrow \pi^0+X$ after the application of such a gate on all telescopes.

Background events are mainly grouped into the window limited by $0 \leq E_\gamma \leq 50$ MeV and $0 \leq m_{inv}c^2 \leq 50$ MeV. They are rather well resolved from the pion decay events which form a broad and strong peak centered at $E_\gamma = 70$ MeV and $m_{inv}c^2 = 35$ MeV. Using a two dimensional free form gate applied in the detected energy vs invariant mass plane, the low invariant mass background present in each detector could easily be rejected. Such a gate is also shown in Figure 12a Figure 12b displays the resulting total invariant mass distribution after a similar gate has been applied for each of the telescopes.

The neutral pion decay kinematics could be used to further improve the background suppression. The $\pi^0 \rightarrow \gamma\gamma$ decays are characterized by a lower limit on the opening angle between the emitted photons. This occurs in symmetrical decays $[E_{\gamma 1} = E_{\gamma 2}]$ for which:

$$\phi_{\gamma 1 \gamma 2} = \phi_{min} = 2\cos^{-1}(\beta_\pi) \qquad (3.3)$$

As an example, for a pion of kinetic energy equal to $T_\pi = m_\pi c^2$, the opening angle $\phi_{\gamma 1 \gamma 2}$, is always higher than $\phi_{min} = 60^o$. The suppression of uncorrelated coincidences that arise either from cosmic showers in the ceiling or fast neutrons seen by the forward detectors could therefore be improved if the events characterized by a too small opening angle were rejected. However, the above equation implies that a gate on $\phi_{\gamma 1 \gamma 2}$ also acts as an upper limit on the kinetic energy of the detected neutral pions. For this reason, the opening angle has been kept free of any constraint in the present analysis.

3.3 *Kinematics.*

Once $\pi^0 \rightarrow \gamma\gamma$ decay events are identified by their invariant mass, the kinematical variables of interest, such as the total energy E_π and the emission angle Θ_π, or correspondingly the transverse momentum p_t and the rapidity y, are derived from the measured energies $E_{\gamma i}$ and laboratory angles $\Theta_{\gamma i}$ of each photon. The total energy is given by:

$$E_\pi = \frac{\sqrt{2} m_\pi c^2}{\left\{ \left(1 - \cos(\phi_{\gamma 1 \gamma 2})\right) \left(1 - \left[\frac{E_{\gamma 1} - E_{\gamma 2}}{E_{\gamma 1} + E_{\gamma 2}} \right]^2 \right) \right\}^{1/2}} \qquad (3.4)$$

where $\phi_{\gamma 1 \gamma 2}$ is the opening angle between the photons in coincidence. Mathematically, (3.4) is identical to $E_\pi = E_{\gamma 1} + E_{\gamma 2}$. However, the above formulation of the pion total energy in terms of the sharing factor, $(E_{\gamma 1} - E_{\gamma 2})/(E_{\gamma 1} + E_{\gamma 2})$, and the known rest mass of the π^0, $m_\pi c^2 = 135$ MeV, offers the advantage of considerably reducing its dependence upon the resolution of the detectors [Ba81]. The kinetic energy of the π^0 simply follows from equation (3.4):

$$T_\pi = E_\pi - 135 \text{ MeV} \qquad (3.5)$$

The emission angle of the pion relative to the beam axis is obtained from the ratio between the parallel component of the detected momentum $p_{//}$, and its total magnitude p_{tot}:

$$\cos(\Theta_\pi) = \frac{p_{//}}{p_{tot}} = \frac{E_{\gamma 1}\cos(\Theta_{\gamma 1}) + E_{\gamma 2}\cos(\Theta_{\gamma 2})}{\left[E_{\gamma 1}^2 + E_{\gamma 2}^2 + 2 E_{\gamma 1} E_{\gamma 2} \cos(\phi_{\gamma 1 \gamma 2}) \right]^{1/2}} \qquad (3.6)$$

Finally, the transverse component of the momentum p_t, and the rapidity y, are derived from E_π and Θ_π using, [Pc87b]:

$$p_t = \frac{1}{c} \sqrt{E_\pi^2 - m_\pi^2 c^4} \; \sin(\Theta_\pi) \qquad (3.7)$$

$$y = \frac{1}{2} \ln\left(\frac{E_\pi + cp_{par}}{E_\pi - cp_{par}}\right) \qquad (3.8)$$

where p_{par} is:

$$p_{par} = \frac{1}{c}\sqrt{E_\pi^2 - m_\pi^2 c^4}\ \cos(\Theta_\pi) \qquad (3.9)$$

From the equations giving E_π and Θ_π, it is clear that the determining factors for their resolution are the detection angles $\Theta_{\gamma 1}$ and $\Theta_{\gamma 2}$ of the π^0 decay photons and the corresponding opening angle $\phi_{\gamma 1 \gamma 2}$. With these considerations, the rather large aperture of the detectors in the reaction plane [$\Delta\Theta = \pm 4^o$ to $\pm 7^o$], could not be omitted in the treatment of the kinematics. When the center coordinates of the telescopes are used to define the emission angle of decay photons, structures appear in the distributions of E_π and Θ_π. In order to correct for this effect, the emission angle $\Theta_{\gamma 1}$, of each decay photon, was randomized over the face of the corresponding telescope. This was achieved using a uniform random distribution of the photon detection coordinates on the converter surface and Euler rotation matrices to treat the geometry. Of course such a procedure does not consider the effect of an asymmetric angular distribution of the pions in the laboratory. However, the former being unknown and in the absence of a better granularity, a uniform smoothing seemed to be an appropriate way to account for the angular distribution of the decay photons in each detector.

Done on a event-by-event basis, this correction does not affect the average kinetic energy and emission angle of a pion if it is repeated several times. To illustrate this point, consider a typical energetic pion decay event where photons of 54 and 256 MeV hit telescopes #4 and #5 respectively. Assuming that these photons were detected at the center of each telescope, the opening angle $\phi_{\gamma 1 \gamma 2}$ is 70^o, leading to a pion of kinetic energy T_π=175 MeV being emitted at 21.5^o in the laboratory. Table 3.1 lists the values of $\phi_{\gamma 1 \gamma 2}$, T_π and Θ_π that were obtained while using 10 different random choices of the photon detection coordinates on the surface of the converters #4 and #5:

Table 3.1: *Effect of the detector apertures on* T_π *and* Θ_π.

	$\phi_{\gamma 1 \gamma 2}$ *(deg)*	Θ_π *(deg)*	T_π*(MeV)*
	67.5	22.3	185
	71.2	22.7	170
	69.7	21.9	176
	66.8	19.7	188
	72.9	23.6	164
	69.9	25.3	175
	70.5	18.5	173
	75.7	23.5	155
	64.3	18.6	199
	74.4	23.9	159
AVRG.	70.3	22.0	174
STRD. DEV.	3.5	2.3	14

Depending on the issue of each random trial for $\Theta_{\gamma 1}$ and $\Theta_{\gamma 2}$, significantly different values of T_π and Θ_π are found; this is reflected in the magnitude of the standard deviations of these variables. However, the exact emission angle of each decay photons being unknown, none of the trials above can be rejected, for they are all consistent with the resolution of the detection setup. Consequently, in the analysis, each π^0 event has been sorted 100 times using different random detection coordinates on the converter face to calculate $\Theta_{\gamma 1}$ and $\Theta_{\gamma 2}$. Each partial outcome was subsequently given a weight of 1/100 in the incrementation of any distribution. The error analysis has also been modified to correctly account for the weight of each partial event. This procedure has for main effect to smooth the data taking into account the finite granularity of the telescopes. This is shown in Figure 13, where are compared the kinetic energy distributions obtained with random $\Theta_{\gamma 1}$ and $\Theta_{\gamma 2}$ sorting the data only once (top) or by summing with equal weights the T_π's resulting from 100 uniform random issues (bottom).

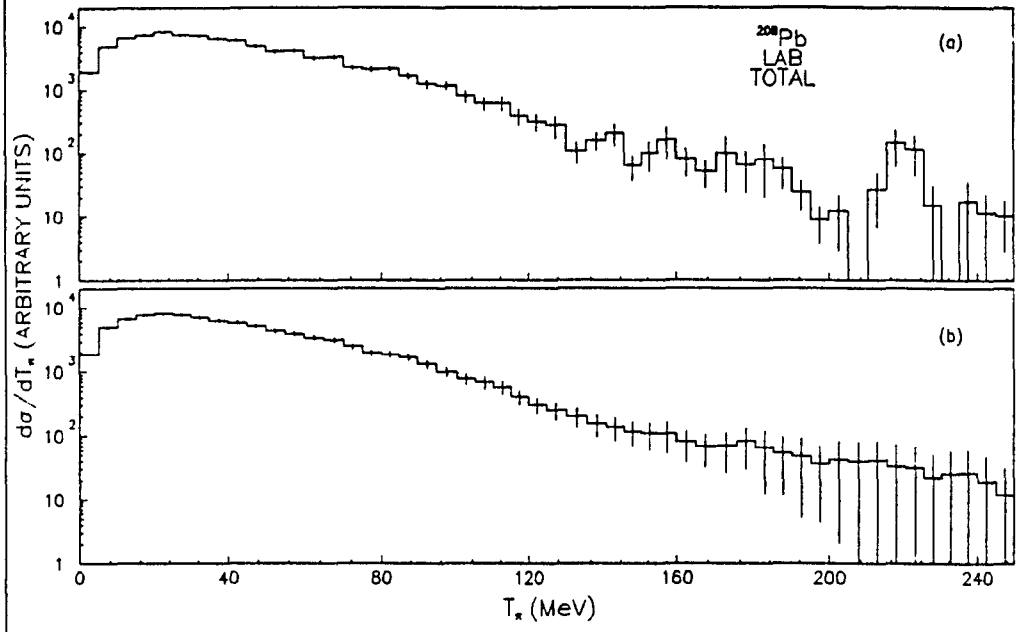

Fig. 13 (top) Kinetic energy distribution obtained when the photon detection coordinates on the converter face are chosen only once at random. (bottom) Same energy distribution when the detection coordinates are chosen randomly 100 times.

As can be seen, the overall shape of the energy distribution is unaffected by the random procedure. The only difference between these two distributions is in the smoother appearance of $d\sigma/dT_\pi$ that results from the 100 trials for $\Theta_{\gamma 1}$ and $\Theta_{\gamma 2}$. In fact, it was verified that a fit of the exponential part of $d\sigma/dT_\pi$ would lead to the same inverse slope parameter and χ^2 regardless of the assumption made on the exact detection coordinates of the decay photons. These two spectra also indicate that above 200 MeV the analysis becomes uncertain, for at these energies the aperture of the telescopes is no longer small compared to $\phi_{\gamma 1 \gamma 2}$. Consequently, the uniform random distribution of each photon on the converter face results in variations of T_π too important to keep faith in the reliability of the method. This is very apparent in the overall trend of the statistical error bars for T_π>180 MeV in Figure 13b. Furthermore, the lack of statistics combined with the presence of remaining background events are sufficient to cause the change in the slope of the energy distribution close to 180 MeV. With prudence, the analysis has thus been limited to pions of kinetic energy below that limit.

3.4 *Energy and Angular Resolutions.*

Because of the experimental geometry that was adopted for this experiment, the pion energy and angular resolutions are determined by several variables. In first order, the intrinsic energy resolution of the lead-glass telescopes as well as their angular aperture will determine the overall trend of the experimental resolution. In addition, because of the nonuniform configuration of the spectrometer in the reaction plane, the resolution also depends upon the emission energy and angle of the pions in the laboratory. Such a multivariable problem can easily be studied with the help of a simulation. Figure 14 shows the logic flow chart of the FORTRAN code based on the Monte Carlo method that was used to study the resolution of the π^0 spectrometer. [This program is a modified version of the code used to evaluate geometrical efficiency discussed in the next section.]

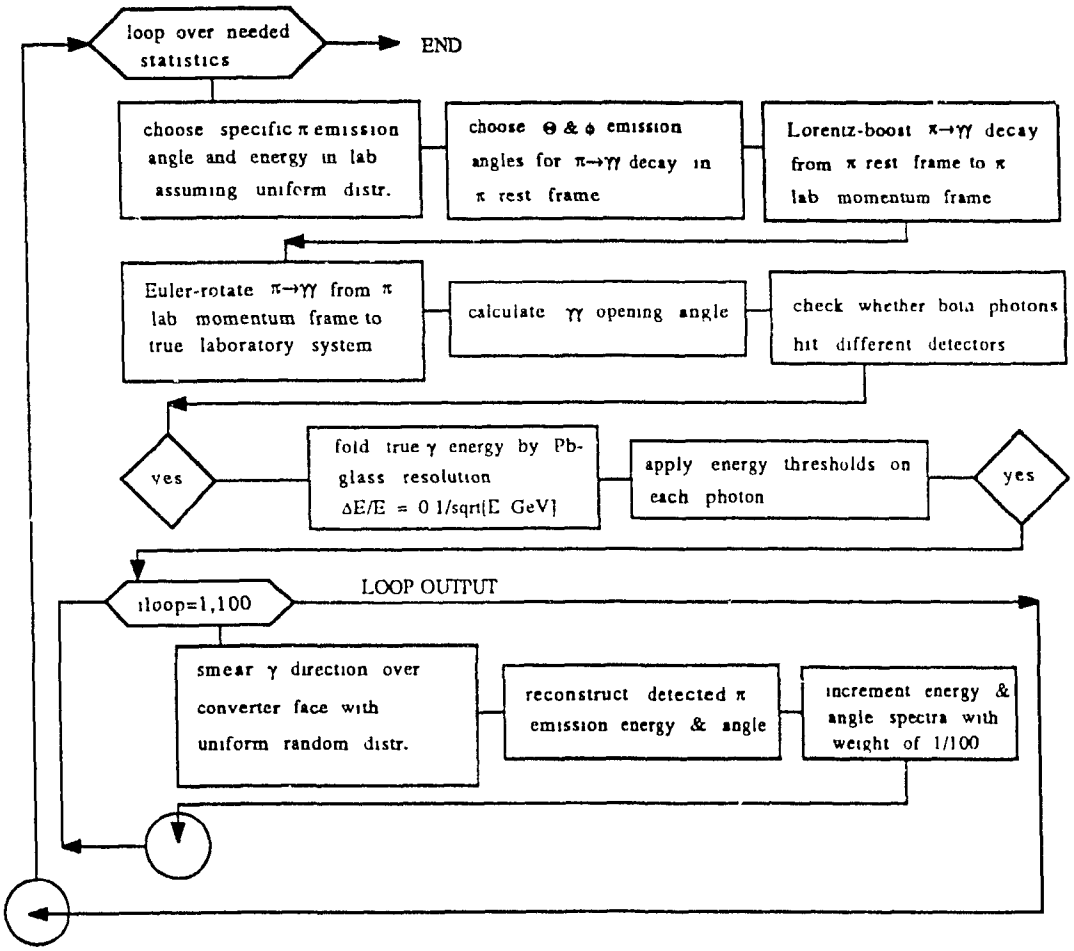

Fig. 14 Logic flow chart of the Monte Carlo simulation used to evaluate the energy and angular resolutions of the detection setup.

Apart from the appropriate kinematical treatment of the $\pi^0 \rightarrow \gamma\gamma$ decay, the two main features of this Monte Carlo are the intrinsic energy resolution function of the Pb-glass detectors and the experimental geometry of the setup including both the laboratory position and the aperture of each telescope. The resolution of the lead-glass detectors for a given photon energy is determined by the statistical fluctuations in the number N of secondary particles contained in the electromagnetic shower [Fa82]. It is therefore characterized by a $1/\sqrt{N}$ dependence. Typically the detector response for photons of energy E_γ is parametrized by a gaussian distribution of Full Width at Half Maximum ΔE_γ given by:

$$\frac{\Delta E_\gamma}{E_\gamma}(\%) = \frac{0.1}{\sqrt{E_\gamma(\mathrm{GeV})}} \qquad (3.10)$$

This behavior of the Pb-glass elements used in the present experiment has been verified using tagged photons by Julien et al. [Ju88b]; they also confirm previous findings by Stachel et al. under similar conditions [St86]. For photons of energy below 50 MeV, the detector response slowly deviates from a gaussian distribution and the resolution $\Delta E_\gamma/E_\gamma$ is better represented by adding an extra small term proportional to $1/E_\gamma$ in equation (3.10). In the present Monte Carlo simulation, this effect has been neglected since the laboratory energy distribution of photons produced in pion decays is peaked around half the π^0 mass, i.e. 70 MeV. As mentioned, the equation giving the total π^0 laboratory energy (3.4) is somewhat sensitive to the opening angle between the decay photons. The angular aperture of each telescope therefore ought to be considered in the evaluation of the overall energy resolution of the detection setup. In order to include this factor and also to stay consistent with the data analysis, the same uniform random angular smoothing of the photon detection angle over the detectors' aperture was used in the Monte Carlo simulation. Figure 15a shows typical angular resolution curves $\Delta\Theta_\pi$ [FWHM] as a function of the input laboratory kinetic energy that is chosen in the very first step of the simulation. Pions emitted at Θ_{lab}=2.5, 72.5, 127.5 and 177.5 degrees are presented. These curves show a rather poor resolution for low kinetic

energy pions as a result of equation (3.10). As expected, the resolution improves for high energies and finally levels off at $\Delta\Theta_\pi \cong 10^o$. This lower limit on the angular resolution is a direct consequence of the aperture of the telescopes.

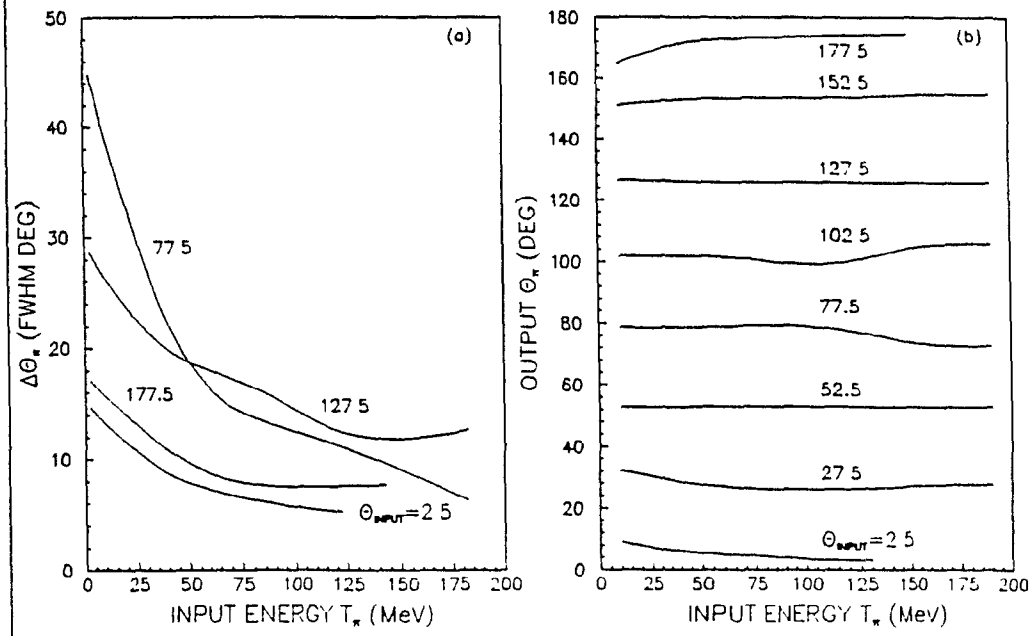

Fig. 15 (a) Estimated angular resolution as a function of the Monte Carlo input emission energy and angle. (b) Reconstructed pion emission angle as a function of the Monte Carlo input emission energy and angle.

Also shown on Figure 15b is the Monte Carlo output emission angle after folding the photon energies with the intrinsic resolution of the detectors, and smearing their emission direction over the converter face. The results are quite satisfactory. In all cases, the average Monte Carlo output emission angle agrees with the input laboratory value of Θ_π to within $\pm 10^o$, which is well inside the limits of the angular resolution.

The results for the kinetic energy resolution are shown in Figure 16a.

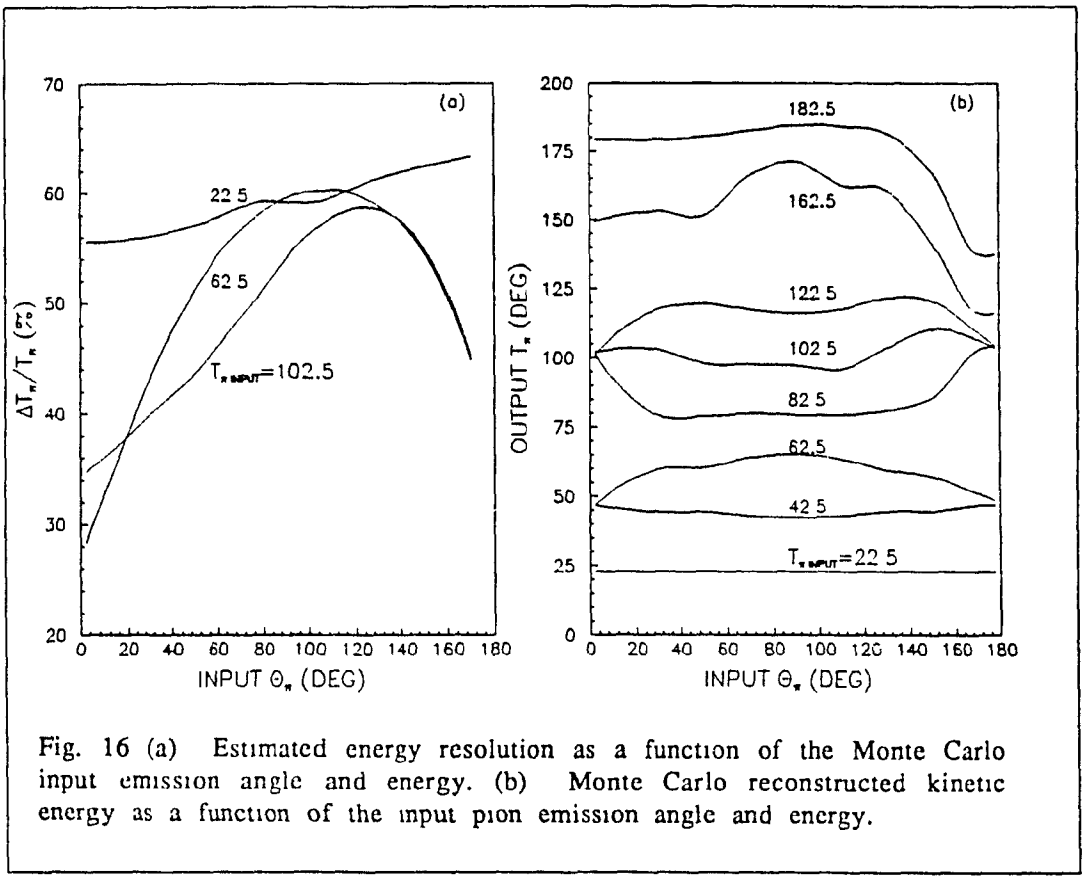

Fig. 16 (a) Estimated energy resolution as a function of the Monte Carlo input emission angle and energy. (b) Monte Carlo reconstructed kinetic energy as a function of the input pion emission angle and energy.

The resolution roughly varies between 40% and 60% depending on Θ_π. For pions emitted with kinetic energy above 50 MeV, $\Delta T_\pi/T_\pi$ is better in the forward and backward directions than at 90°. For forward pions, this is due to the opening angle and the distances chosen for telescopes #4 & #5. In the backward direction, the slight deterioration of resolution as compared to the forward case, results from the closer distances between the target and detectors #1 & #8. For pions of lower kinetic energy, the opening angle between each detector is no longer a determining factor in the resolution, for the distribution of decay photons is roughly isotropic in the laboratory. Therefore in this case, the energy resolution is mainly affected by the telescope distance distribution. This is clearly shown on Figure 16a by the resolution curve for T_π=22.5 MeV. At this energy, the resolution is almost constant. [In fact, it is slightly higher in the backward direction due to the

smaller target to detector distances in that region.] The Monte Carlo output kinetic energies as a function of the laboratory emission angle of the pions are shown in Figure 16b. In the range $25^{o} \leq \Theta_{\pi} \leq 140^{o}$, the Monte Carlo output values agree well with the input ones. However, one observes an apparent degeneracy of these curves near $\Theta_{\pi}=0^{o}$ and $\Theta_{\pi}=180^{o}$ for pions above 50 MeV. This arises because most of the forward (backward) energetic pions are detected by a single pair of detectors, namely #4 & #5 (#1 & #8). The effect on the data of this degeneracy depends strongly upon the experimental energy and angular distributions of the pions. For instance, only a few pions of $T_{\pi} \geq 60$ MeV are detected backward in the laboratory [see Figure 23]. The predicted nonlinearity at forward angles should result in peaks in the kinetic energy spectrum at 50 and 100 MeV However, this effect is considerably reduced by the large experimental resolution on the pion emission angle. This is shown on Figure 34 in chapter 5, where the laboratory kinetic energy distributions of pions emitted in the angular range $0^{o} \leq \Theta_{\pi} \leq 30^{o}$ are displayed for all three targets. It can be seen that, these distributions are free of any structure at 50 and 100 MeV.

3.5 *Cross Section Normalization.*

The absolute cross section normalization has been obtained by giving a proper detection weight $d\sigma$ to each event recognized as a good $\pi^0 \rightarrow \gamma\gamma$ decay. For that purpose, one has to evaluate the total probability $\varepsilon_c(E_{\gamma 1})\varepsilon_c(E_{\gamma 2})$ that photons of energy $E_{\gamma 1}$ and $E_{\gamma 2}$ will produce a signal above threshold in each Pb-glass element of a telescope, and the probability $\varepsilon_g(T_\pi, \Theta_\pi)$, that the corresponding π^0 decay photons will hit two different detectors of the spectrometer. Once these probabilities are known, the relative normalization of each π^0 event is given by:

$$d\sigma \alpha \left[\varepsilon_c(E_{\gamma 1})\,\varepsilon_c(E_{\gamma 2})\,\varepsilon_g(T_\pi, \Theta_\pi)\right]^{-1} \qquad (3.11)$$

As displayed in Figure 17, the geometrical efficiency $\varepsilon_g(T_\pi, \Theta_\pi)$, has been evaluated via a Monte Carlo simulation† handling the π^0 decay kinematics in a way that is very similar to the resolution simulation discussed in the previous section.

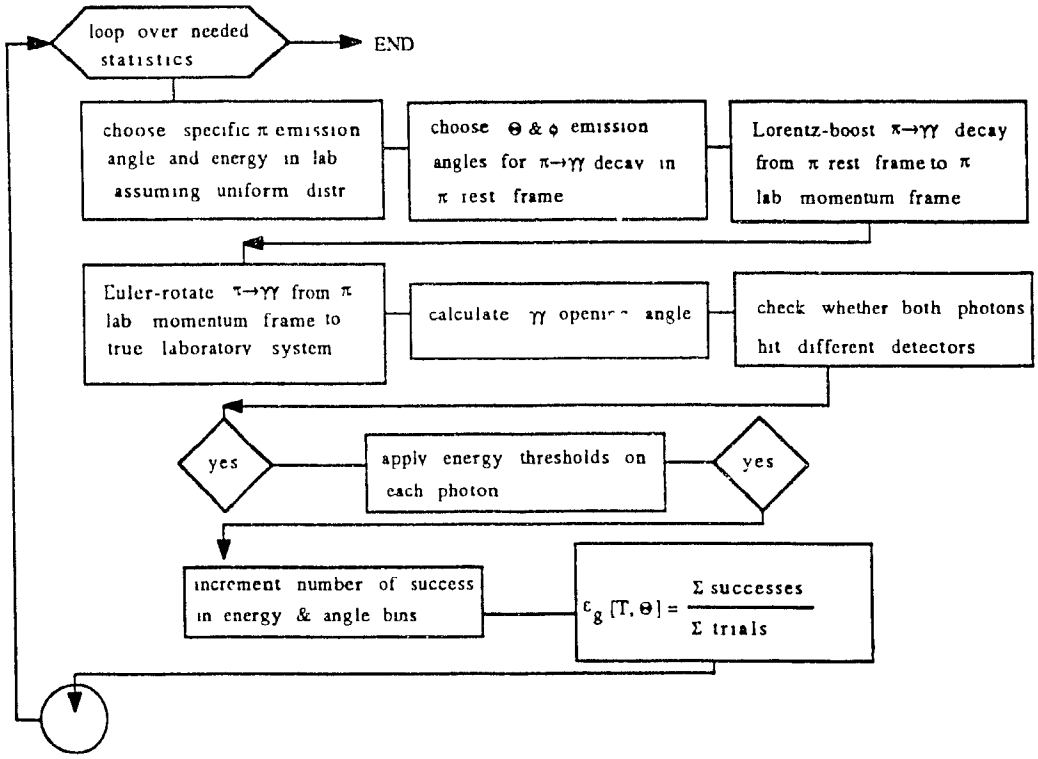

Fig. 17 Logic flow chart of the Monte Carlo simulation used to evaluate the geometrical detection efficiency of the neutral pion spectrometer.

† The author acknowledges P. Braun-Munzinger for the loan of this program.

This simulation called for a number of 15000 successes in each angle integrated energy bin. The uncertainty on $\varepsilon_g(T_\pi,\Theta_\pi)$ arising from the limited statistics has been taken into account in the event-by-event error analysis [see section 3.6]. In Figure 18, the result of this simulation is presented as a linear 3 dimensional surface plot in the T_π vs Θ_π plane.

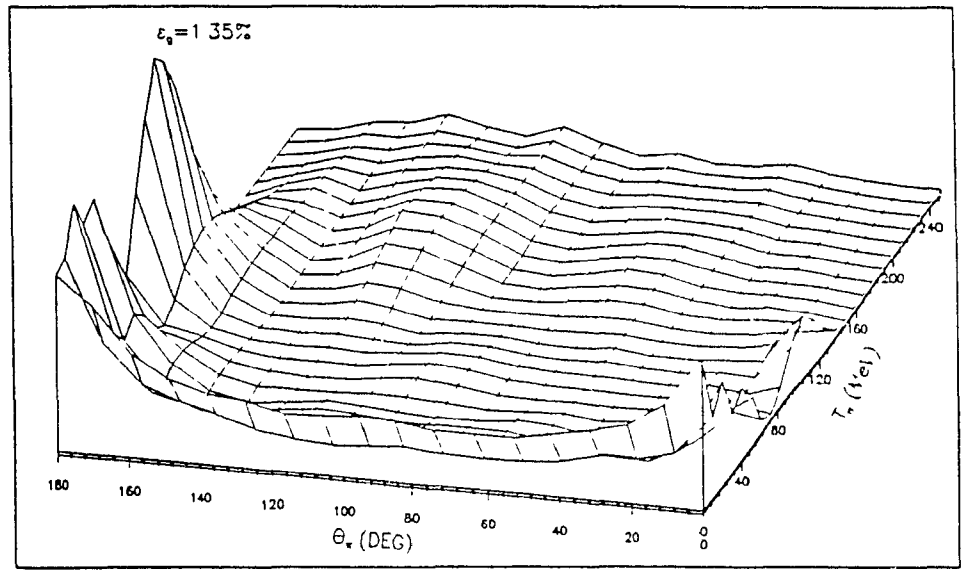

Fig. 18 Three dimensional view of the geometrical detection efficiency of the detection setup in the kinetic energy vs emission angle plane.

In the valley limited by $T_\pi \geq 80$ MeV and $30 \leq \Theta_\pi \leq 150^o$, $\varepsilon_g(T_\pi,\Theta_\pi)$ is almost uniform and typically equal to 0.1%. The important forward and backward peaks are attributable to the geometrical configuration of the spectrometer. Firstly, the distribution of relative opening angle between all possible pairs of detectors does not cover uniformly the angular range $0^o \leq \phi_{\gamma 1 \gamma 2} \leq 180^o$ and is more sensitive to pions emitted in the regions $0^o \leq \Theta_\pi \leq 30^o$ and $150^o \leq \Theta_\pi \leq 180^o$ than to those emitted at $\Theta_\pi = 90^o$. In addition, because the detectors #4 & #5 are twice as far from the target than the pair #1 & #8 [see Table 2.1], the efficiency to pions emitted backward is on average higher than for those emitted in the forward direction.

The geometrical efficiency $\varepsilon_g(T_\pi,\Theta_\pi)$, does not take into account the finite detection efficiency of the telescopes for γ-rays. Hence, in evaluating the total detection probability of each $\pi^0 \rightarrow \gamma\gamma$ events, one must multiply $\varepsilon_g(T_\pi,\Theta_\pi)$ by the probability that both photons will lead to signals above threshold in the converter and absorber. The conversion efficiency $\varepsilon_c(E_\gamma)$, as just defined, is for each telescope, a function of the incoming photon energy and of the thresholds applied on the Pb-glass detectors. Because the incoming photon energy must be known beforehand, the conversion efficiency is measured using tagged photons beam. For the present Pb-glass Cherenkov counters, this has been done at the 600 MeV Saclay electron LINAC with tagged photons of 20 to 100 MeV [Ju88a, Ju88b], using hardware thresholds of 5 and 10 MeV on the converter and absorber respectively. The resulting experimental curve is shown in Figure 19.

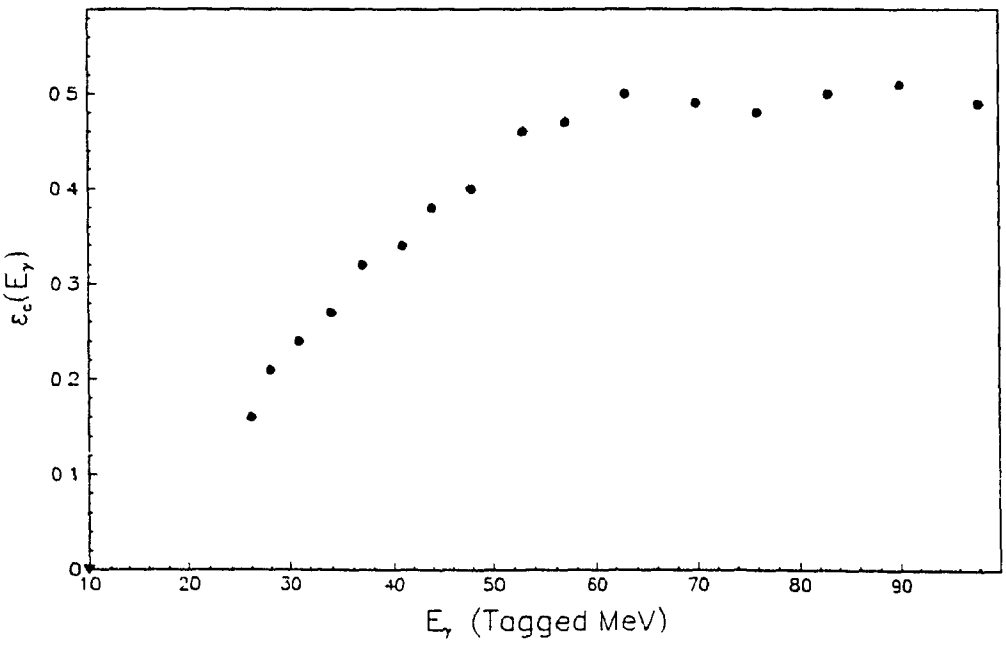

Fig. 19 Measured conversion efficiency with respective hardware thresholds of 5 and 10 MeV on the Pb-glass converter and absorber. After the work of J. Julien et al. [Ju88b].

In the present analysis, the measured conversion efficiency has been smoothed between 26 and 100 MeV. Also, in the absence of any data points lower than 26 MeV, the $\varepsilon_C(E_\gamma)$ curve was linearly extrapolated assuming that it vanishes for photon energies equal to the total detector threshold, i.e. E_γ=15 MeV. The fluctuations of ± 0.02 observed above E_γ=70 MeV are representative of the experimental error on the measurement. Hence, for photon energies higher than that value, a constant of 0.5 was used for the conversion efficiency

The sensitivity of this curve to the experimental thresholds has been studied using single γ-ray spectra measured with a multiplicity $M \geq 1$ acquisition trigger In a given telescope, any variation of the single photon energy distribution for different converter and absorber thresholds can only be due to the dependence of the detection probability $\varepsilon_C(E_\gamma)$ upon these. Hence, by observing the change of the single photon spectrum measured in any detector under two different sets of converter and absorber thresholds, one directly obtains the corresponding variation of the conversion efficiency The threshold fluctuations of the γ-ray detection probability were thus studied using telescope #7 of the setup, characterized by the lowest threshold values for both Pb-glass elements [see Table 2.1]. The study was accomplished by taking the ratio $R(E_\gamma, Thr_{C1}, Thr_{A1}; Thr_{C2}, Thr_{A2})$ between the photon spectrum obtained in this telescope by applying a given set of converter and absorber software thresholds Thr_{C1} & Thr_{A1} and the same spectrum, this time gated by Thr_{C2}=5 MeV and Thr_{A2}=10 MeV

The resulting curves, shown in Figure 20, display the strong sensitivity of the conversion efficiency to threshold variations One can see that modifications of the converter and absorber thresholds have different effects on the γ-ray detection probability. In Figure 20a, where only Thr_{A1} varies, these curves show that the absorber threshold acts mainly like a sharp cutoff on the photon yield at low energies and does not affect photons of energy higher than 100 MeV, R being asymptotic to 1 above that value. For the converters, the situation is different.

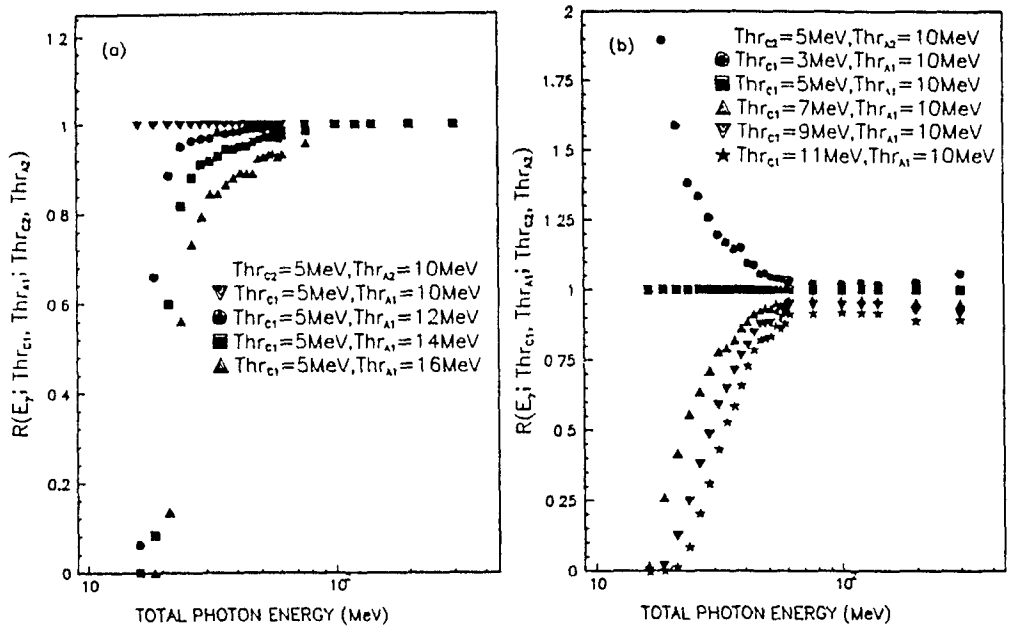

Fig. 20 (a) Evolution of the photon detection efficiency as function of absorber thresholds. (b) Evolution of the photon detection efficiency as function of converter thresholds.

Part (b) of Figure 20 shows that a steady augmentation of the converter threshold attenuates the photon detection efficiency over the entire energy range. In spite of the observed sensitivity of the detection efficiency at low energies, it is satisfying to see that above E_γ=70 MeV, the detection probability appears to be quite independent of the thresholds.

According to the above discussion, the effects of different discriminator thresholds Thr_{C_i} & Thr_{A_i} applied on the Pb-glass components of a telescope i, were accounted for in the analysis by multiplying the experimental conversion efficiency of Figure 19 by $R(E_\gamma; Thr_{Ci}, Thr_{Ai}; 5\ MeV, 10\ MeV)$.

Once the relative normalization $d\sigma$ was known, a final rejection criterion was applied on the statistics. Among all $\pi^0 \rightarrow \gamma\gamma$ events, those which are characterized by very low total detection efficiency lead to unacceptably large contributions to the overall cross section. They are also more likely to be contaminated by various background counts due to their low probability of occurrence. In order to minimize the impact of these low efficiency contributions on the differential distributions,

any event for which the total detection efficiency $\varepsilon_c(E_{\gamma 1})\varepsilon_c(E_{\gamma 2})\varepsilon_g(T_\pi,\Theta_\pi)$ was lower than 1.6×10^{-5} was rejected. For each target the number of events rejected in this manner accounts for less than 0.5% of the $\pi^0\rightarrow\gamma\gamma$ statistics. The gating was mainly effective for kinetic energies above 150 MeV, which were not considered in the remainder of the analysis. Finally, the value of the total cross section was corrected to account for this cut.

3.6 *Experimental Distributions.*

Neutral pion cross sections are best presented in the full phase space using the Lorentz-invariant doubly differential cross-section:

$$\sigma_{inv} = E_\pi \frac{d^3\sigma}{d^3\vec{p}} = \frac{1}{p}\frac{d^2\sigma}{dT_\pi d\Omega} = \frac{1}{2\pi p_t}\frac{d^2\sigma}{dp_t dy} \qquad (3.12)$$

where p is the total momentum, and E_π the total energy of the pion. In this event-by-event analysis, every $\pi^0 \rightarrow \gamma\gamma$ decay was calculated 100 times choosing, for each photon, uniform random detection coordinates on the corresponding converter face. Each resulting outcome i, has accordingly received the following absolute weight:

$$d\sigma_i(T_{\pi i},\Theta_{\pi i}) = w\frac{10^{30}}{N_p N_t}\left[\varepsilon_c(E_{\gamma 1})\,\varepsilon_c(E_{\gamma 2})\,\varepsilon_g(T_{\pi i},\Theta_{\pi i})\right]^{-1} \qquad (3.13)$$

where the factor w arises from the uniform random smooth over the detector apertures and is equal to 1/100. When N_p and N_t, which correspond respectively to the integrated beam current and the target thickness, are expressed in their proper units, $d\sigma_i$ is given in micro barns.

The total quadratic error contribution of each outcome is given by:

$$\left[\frac{\Delta(d\sigma_i(T_{\pi i},\Theta_{\pi i}))}{d\sigma_i(T_{\pi i},\Theta_{\pi i})}\right]^2 = w\left[1 + \left|\frac{\Delta(\varepsilon_g(T_{\pi i},\Theta_{\pi i}))}{\varepsilon_g(T_{\pi i},\Theta_{\pi i})}\right|^2\right] \qquad (3.14)$$

In equation (3.14), w is once again used to weight the contribution of the outcome i. The constant 1 in the square brackets properly accounts for the intrinsic statistical uncertainty of each $\pi^0 \rightarrow \gamma\gamma$ event. The uncertainty resulting from the Monte Carlo evaluation of the geometrical efficiency was also added quadratically in the computation of the total error contribution.

To remain consistent with the resolution of the detection setup, the bin widths have been chosen to be equal to dT_π=10 MeV, $d\Omega$=10°,

dp_t=10 MeV/c and dy=0.2 units of rapidity. Also, as already mentioned, the analysis has been limited to neutral pions of kinetic energy lower than 180 MeV, since the granularity of the π^0 spectrometer was not sufficient to allow a proper detection of higher energy events.

The Lorentz transformation of the results from the laboratory to any other inertial system moving with a velocity β_F along the positive beam axis, is easily achieved by using the invariant cross section σ_{inv}. According to equation (3.12) one has:

$$\sigma_{inv} = \frac{1}{p^{lab}} \frac{d^2\sigma}{dT_\pi^{lab} d\Omega^{lab}} = \frac{1}{p^F} \frac{d^2\sigma}{dT_\pi^F d\Omega^F} \qquad (3.15)$$

or additionally:

$$\sigma_{inv} = \frac{1}{2\pi p_t^{lab}} \frac{d^2\sigma}{dp_t^{lab} dy^{lab}} = \frac{1}{2\pi p_t^F} \frac{d^2\sigma}{dp_t^F dy^F} \qquad (3.16)$$

The distributions of the relevant variables such as T_π^F, Θ_π^F or y^F, are then obtained by the integration of equations (3.15) or (3.16). For instance, the kinetic energy distribution in the frame F is given by:

$$\frac{d\sigma}{dT_\pi^F} = \int p^F \left(\frac{1}{p^{lab}} \frac{d^2\sigma}{dT_\pi^{lab} d\Omega^{lab}} \right) d\Omega^F \qquad (3.17)$$

while the rapidity distribution is obtained by:

$$\frac{d\sigma}{dy^F} = \int 2\pi p_t^F \left(\frac{1}{2\pi p_t^{lab}} \frac{d^2\sigma}{dp_t^{lab} dy^{lab}} \right) dp_t^F \qquad (3.18)$$

In an event-by-event analysis, the integration symbol stands for the incrementation of the distribution in the appropriate bin by a weight equal to the integrand of equation (3.17) or (3.18).

All kinematical variables are easily transformed from the laboratory to a moving frame F using Lorentz transformation rules expressed in terms of a rapidity boost. For a particle moving along the positive laboratory z axis with a velocity β_{lab}, one can write [Se77]:

$$\beta^{lab} = \tanh\left(y^{lab}\right) \tag{3.19}$$

and:

$$\gamma^{lab} = \left[1 - \left(\beta^{lab}\right)^2\right]^{-1/2} = \cosh\left(y^{lab}\right) \tag{3.20}$$

The components of the particle's 4-momentum $(E_\pi{}^{lab}, p^{lab})$ are then given by:

$$E_\pi^{lab} = m_\perp c^2 \cosh\left(y^{lab}\right) \tag{3.21}$$

$$cp_{par}^{lab} = m_\perp c^2 \sinh\left(y^{lab}\right) \tag{3.22}$$

$$p_t^{lab} = p_t \tag{3.23}$$

where:

$$m_\perp c^2 = \sqrt{m_\pi^2 c^4 + c^2 p_t^2} \tag{3.24}$$

While moving from the laboratory to a frame F by a boost β^F along the positive beam axis, the particle's rapidity in F is given by the simple relation:

$$y^F = y^{lab} - u^F \tag{3.25}$$

with u^F being:

$$u^F = \tanh^{-1}\left(\beta^F\right) \tag{3.26}$$

In that new frame, the 4-momentum components now become:

$$E_\pi^F = m_\perp c^2 \cosh\left(y^F\right) \tag{3.27}$$

$$cp_{par}^F = m_\perp c^2 \sinh\left(y^F\right) \tag{3.28}$$

$$p_t^F = p_t^{lab} \tag{3.29}$$

Hence, the transformation of the $\pi^0 \rightarrow \gamma\gamma$ kinematics to a frame F such as the nucleus-nucleus center of mass, is simply achieved by subtracting from the laboratory rapidity of the pion, the rapidity u^F of that frame, and by using equations (3.27) to (3.29) to obtain the transformed 4-momentum. From these, $T_\pi{}^F$, and $\Theta_\pi{}^F$ are straightforward to compute and their distribution is found by integration of the invariant cross section, as already discussed.

CHAPTER 4

RESULTS

A survey of the experimental results is given in this chapter. The presentation is limited here to the main characteristics of subthreshold pion production at 95 MeV/u, and it will be shown that these data nicely follow the results obtained at lower beam energies. The theoretical interpretation has been saved for the next chapter.

4.1 Total Cross Sections and Mass Dependence.

Table 4.1 lists the total inclusive production cross sections obtained for the three targets studied in the present experiment.

Table 4.1: *Total production cross sections.*

Target	σ_{tot} *(μbarns)*	$\sigma_{tot}/(A_p A_t)^{2/3}$
^{208}Pb	490 ± 8 ± 98	2.2
^{58}Ni	262 ± 4 ± 52	2.8
^{27}Al	175 ± 4 ± 35	3.1

Two contributions are quoted for the total error. The first one is the statistical uncertainty on the data as obtained from equation (3.14), while the second arises from a 10% uncertainty on the absolute normalization of the conversion efficiency presented in Figure 19. Referring to the third column of Table 4.1, one also sees that at E_{lab}/A=95 MeV/u, the ratio $\sigma_{tot}/(A_p A_t)^{2/3}$ has an average value of 2.7 μb, which is in the continuation of the experimental excitation function that was presented in Figure 1.

The power law behavior of the integrated pion production cross section is presented on Figure 21, where σ_{tot} is plotted on a log-log scale as a function of the product of the target and projectile masses A_pA_t. Using a linear regression, the mass dependence of our data is best given by $\sigma_{tot}\alpha(A_pA_t)^{0.51}$. This result can be understood in the following way. At 95 MeV/u, pions are not predominantly created at the surface by first chance nucleon-nucleon interactions, which would result in $\sigma_{tot}\alpha(A_pA_t)^{2/3}$, but would rather originate from an extended source formed by the nucleons enclosed in the overlapping volume between the target and the projectile nuclei. In this geometry, the cross section is expected to scale roughly as $(A_p^{1/3}A_t^{2/3} + A_p^{2/3}A_t^{1/3})$ [St86] The experimental mass dependence of the total cross section agrees quite well with the prediction of this scaling law which is shown in Figure 21 as a solid line normalized to the measured cross section of ^{27}Al.

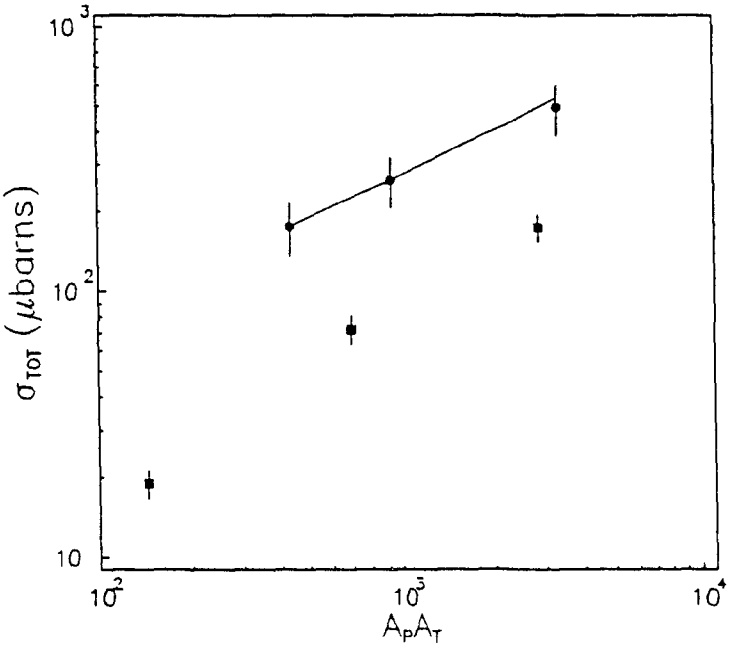

Fig. 21 Mass dependence of the integrated pion production cross sections; full circles: present experiment; full squares: $^{12}C+^{12}C$, ^{58}Ni, ^{238}U at 84 MeV/u [No84]. The full line corresponds to $\sigma\alpha(A_t^{2/3}A_p^{1/3}+A_t^{1/3}A_p^{2/3})$.

The results can also be compared to those obtained for an E_{lab}/A=85 MeV/u ^{12}C projectile [No84]. The observed mass dependence

of both of these measurements agrees well for heavy targets. However, at 85 MeV/u, one observes a significant breakdown in the trend of σ_{tot} for the light system $^{12}C+^{12}C$. Two phenomena may account for this effect. Firstly, for a light system like $^{12}C+^{12}C$, the reaction may well be dominated by skin effects due to the small size of both colliding nuclei. However, such an effect seems to be much weaker for the light system $^{16}O+^{27}Al$ at 95 MeV/u. This could be due to the higher beam energy, which is more likely to create a larger interaction volume between the two colliding nuclei. Secondly, one could consider the reabsorption of pions after their production as being responsible for an increasing attenuation of σ_{tot} as the colliding system grows in mass. The system $^{12}C+^{12}C$ at 85 MeV/u would then be the least affected by this effect and all other systems presented in Figure 21 would be faint "images" of the primary production cross section.

4.2 *Kinetic Energy Distributions.*

Figure 22 presents the angle integrated kinetic energy distributions measured in the laboratory for all three targets. The experimental spectra peak between 20 and 30 MeV and then fall off almost exponentially.

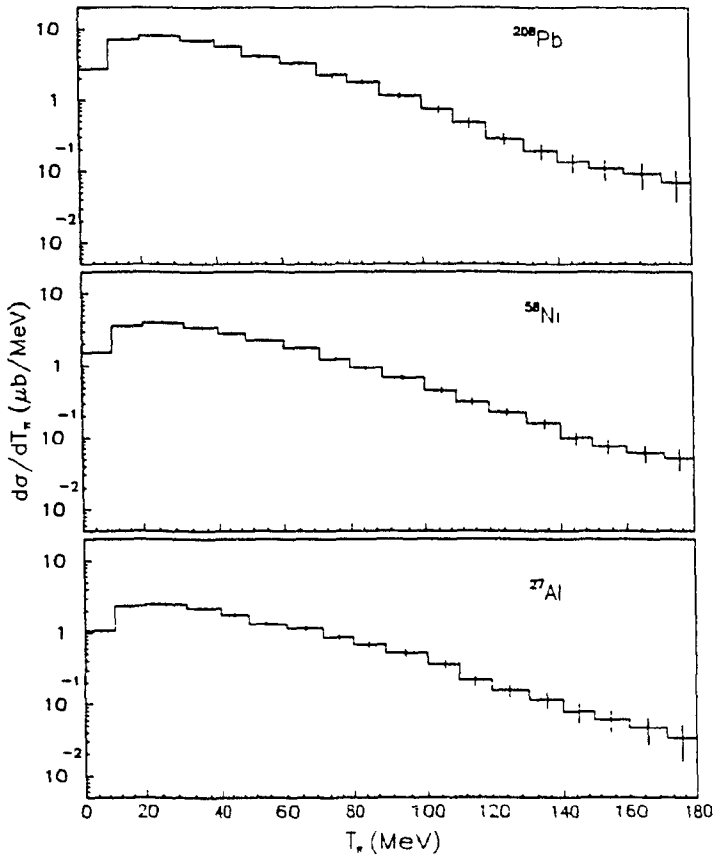

Fig. 22 Laboratory kinetic energy distributions of pions produced in the reactions $^{16}O+^{27}Al$, ^{58}Ni, $^{208}Pb \rightarrow \pi^0+X$ at 95 MeV/u.

Table 4.2 lists the inverse slope parameters E_0, found for the three targets by fitting the spectra between 50 MeV and 150 MeV according to the ansatz $d\sigma/dT_\pi \alpha \exp(-T_\pi/E_0)$. This table gives the inverse slope parameters obtained for the angle integrated kinetic energy distributions, as well as those for pions emitted in the forward

($0^o \leq \Theta_\pi \leq 30^o$), sideward ($60^o \leq \Theta_\pi \leq 120^o$), and backward ($150^o \leq \Theta_\pi \leq 180^o$) angular regions of the laboratory. The error bars quoted are the standard deviations on the χ^2 fit. For later use, the E_0's resulting after transformation of the distributions to the nucleus-nucleus center of mass (CM), the "average source" rest frame (SO) [see $\beta_{0\text{-}30}$ next section], and the free nucleon-nucleon system (NN) are also presented.

Table 4.2: *Experimental inverse slope parameters.*

		^{208}Pb		
emis. angle.	$E_{0\ LAB}$(MeV)	$E_{0\ CM}$(MeV)	$E_{0\ SO}$(MeV)	$E_{0\ NN}$ (MeV)
$0^o \leq \Theta_\pi \leq 180^o$	26.9±0.9	26.5±0.9	26.7±0.9	30.3±1.1
$0^o \leq \Theta_\pi \leq 30^o$	35.0±2.6	32.3±2.7	31.3±3.5	29.9±5.6
$60^o \leq \Theta_\pi \leq 120^o$	25.1±1.3	25.8±1.3	23.8±2.2	26.6±1.5
$150^o \leq \Theta_\pi \leq 180^o$	21 5±2.0	22.6±2.0	25.4±1.3	37.2±3.0
frame velocity	β_{LAB}=0.0	β_{CM}=0.03	β_{SO}=0.10	β_{NN}=0.22
		^{58}Ni		
emis. angle.	$E_{0\ LAB}$(MeV)	$E_{0\ CM}$(MeV)	$E_{0\ SO}$(MeV)	E_{0NN} (MeV)
$0^o \leq \Theta_\pi \leq 180^o$	29 8±0.8	28.0±0.8	28.4±0.8	29.7±0.8
$0^o \leq \Theta_\pi \leq 30^o$	44 9±2.8	39.3±3.1	36.8±3.5	28.9±2.8
$60^o \leq \Theta_\pi \leq 120^o$	25.7±1.0	26.1±1.0	26.4±0.3	28.2±1.1
$150^o \leq \Theta_\pi \leq 180^o$	17.3±0.9	20.6±1.0	27.0±1.0	28.4±1.4
frame velocity	β_{LAB}=0.0	β_{CM}=0.10	β_{SO}=0.15	β_{NN}=0.22
		^{27}Al		
emis. angle	$E_{0\ LAB}$(MeV)	$E_{0\ CM}$(MeV)	$E_{0\ SO}$(MeV)	E_{0NN} (MeV)
$0^o \leq \Theta_\pi \leq 180^o$	32.9±1.5	28.8±1.3	28.8±1.3	29.3±1.7
$0^o \leq \Theta_\pi \leq 30^o$	56.8±6.7	35.4±4.7	30.9±3.7	24.2±2.8
$60^o \leq \Theta_\pi \leq 120^o$	25.0±1.6	24.7±1.0	24.8±2.9	27.1±1.7
$150^o \leq \Theta_\pi \leq 180^o$	17.6±1.8	26.7±2.5	26.9±1.6	30.7±3.0
frame velocity	β_{LAB}=0.0	β_{CM}=0.17	β_{SO}=0.18	β_{NN}=0.22

The angle integrated values obtained in the laboratory are in good agreement with those observed at 84 MeV/u for the reactions $^{12}C+^{238}U$, ^{58}Ni, ^{12}C. For these systems, Noll et al. [No84] have reported inverse slopes parameters of 26±2 MeV, 27±2 MeV and 28±2 MeV respectively.

This table also clearly displays the strong dependence of E_0 on the reaction kinematics in the forward and backward directions. However, as expected, when transformed to different inertial frames, the slope of the sideward pion energy distributions is not affected. One notes that the E_0's obtained from these spectra are very close to the constant value of 22±2 MeV found at beam energies below 60 MeV/u [see Figure 2]. Moreover, at 90° the π^0 kinetic energy distributions have very similar slopes for all three targets. This rather surprising result will be discussed further in the next chapter in the framework of the thermal source model.

4.3 *Angular Distributions.*

The energy integrated angular distributions for the three reactions studied in the present experiment are presented in Figure 23. For each target, $d\sigma/d\Omega$ is shown in the laboratory, the nucleus-nucleus (CM), and the nucleon-nucleon (NN) center of mass rest frames. The velocities of these specific inertial systems are listed in Table 4.3.

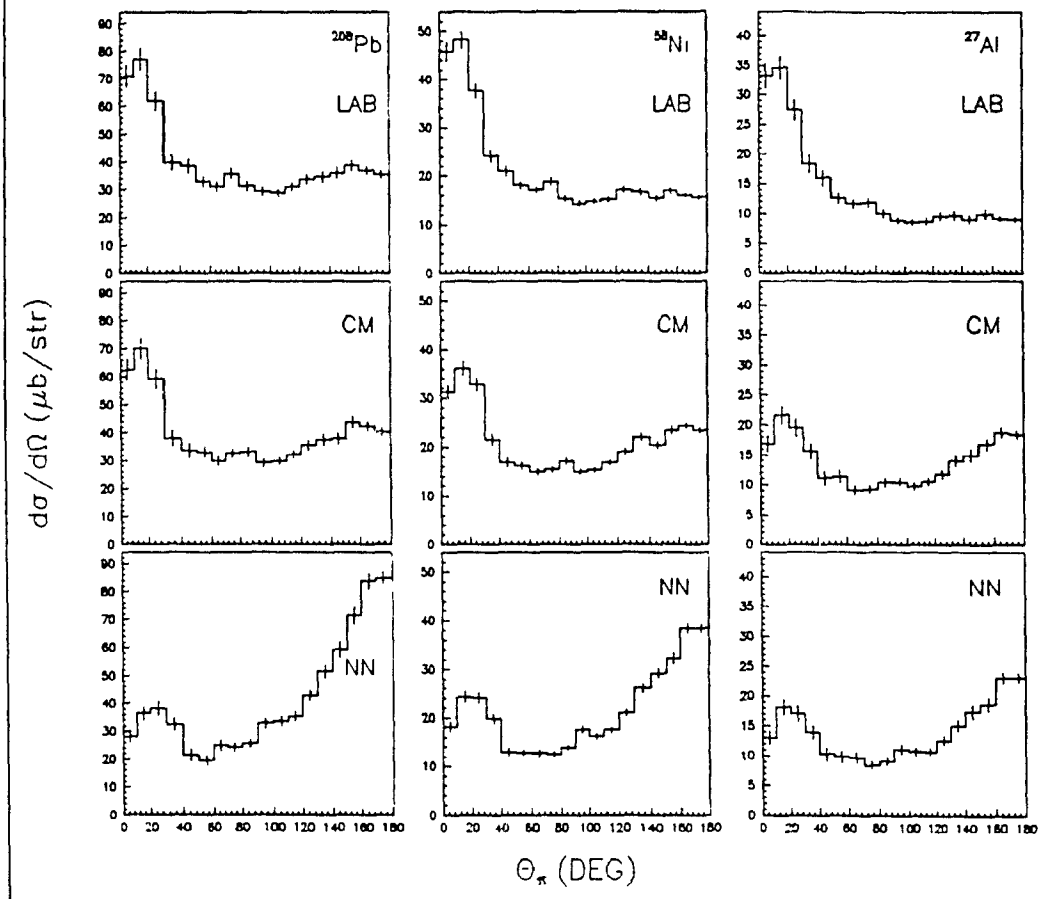

Fig. 23 Angular distributions of pions produced in the reactions $^{16}O+^{27}Al$, ^{58}Ni, $^{208}Pb \rightarrow \pi^0+X$ at 95 MeV/u. CM corresponds to the nucleus-nucleus center of mass frame; NN to the nucleon-nucleon system.

The laboratory distributions are strongly peaked in the forward direction. In this frame, the ratio of the forward ($\Theta_\pi \leq 10^o$) to backward ($\Theta_\pi \geq 170^o$) bins equals 2.0 for ^{208}Pb, 2.9 for ^{58}Ni, and 3.7 for ^{27}Al. The transition from forward to backward peaked distributions as one

transforms $d\sigma/d\Omega$ from the nucleus-nucleus center of mass to the nucleon-nucleon rest frame is an indication that the apparent production source moves with a velocity between β_{CM} and β_{NN}. One also notes that in all inertial frames, the angular distributions are anisotropic. As will be discussed in the next chapter, this requires that in its own rest frame, the average pion source emission is characterized by an intrinsic p-wave component.

For asymmetric colliding systems, requiring the energy integrated angular distribution to be forward-backward symmetric allows a first order determination of the average π^0 source's rest frame velocity. Such a symmetrical angular distribution is obtained by applying a Lorentz boost β_{SO}, leading to equal integrated cross sections in the forward and backward hemispheres, i.e. $\sigma(0^o \rightarrow 90^o) = \sigma(90^o \rightarrow 180^o)$. Because of the large solid angle covered by an angular bin in the sideward region, it is clear that a symmetrization of $d\sigma/d\Omega$ over the full Θ_π range will give much more weight to the pions emitted at 90^o. Figure 23 shows that in the sideward region, $d\sigma/d\Omega$ is unaffected by a Lorentz transformation compared to the forward and backward parts. Hence, while looking for a velocity boost satisfying the equality $\sigma(0^o \rightarrow 90^o) = \sigma(90^o \rightarrow 180^o)$, the answer is only determined by very small differences in the total cross section, since the bins having the largest weight are also those which are not affected by Lorentz transformations. A more sensitive symmetrization criterion requires the equality of the integrated cross sections only in some restricted forward and backward ranges such as those covered by $0^o \leq \Theta_\pi \leq 30^o$ and $150^o \leq \Theta_\pi \leq 180^o$. In Table 4.3, the source velocities $\beta_{0\text{-}90}$ and $\beta_{0\text{-}30}$, obtained from the angular distributions by applying respectively the criteria $\sigma(0^o \rightarrow 90^o) = \sigma(90^o \rightarrow 180^o)$ and $\sigma(0^o \rightarrow 30^o) = \sigma(150^o \rightarrow 180^o)$, are listed for each target. In addition, the velocities corresponding to the centroid of the laboratory rapidity distributions β_y are provided [see next section]. For comparison purposes, the nucleus-nucleus center of mass and the nucleon-nucleon frame velocities β_{CM} and β_{NN} are also given.

Table 4.3: *Extracted source velocities.*

Vel.	^{208}Pb	^{58}Ni	^{27}Al
β_{CM}	0.03	0.10	0.17
$\beta_{0\text{-}90}$	0.06	0.11	0.17
β_y	0.07	0.12	0.17
$\beta_{0\text{-}30}$	0.10	0.15	0.18
β_{NN}	0.22	0.22	0.22

If the pions had originated from a single unperturbated source, the apparent velocity would have been independent of whether it was obtained by symmetrizing the angular distribution over a given Θ_π range or from the centroid of the rapidity distribution. As will be discussed in the next chapter, it is believed that the difference between $\beta_{0\text{-}90}$, β_y, and $\beta_{0\text{-}30}$ arises from the effect of reabsorption on the primary pions as they pass through the surrounding matter after their emission. Under such considerations, the best estimate of the source velocity would be $\beta_{0\text{-}30}$, since the forward and backward angular regions are the most sensitive to any change in the frame velocity.

Independent of the method, source velocities significantly lower than that of the nucleon-nucleon frame are found for each target. This fact may be an indication that cooperative mechanisms still dominate the neutral pion production at 95 MeV/u. A π^0 production originating predominantly from single first chance nucleon-nucleon collisions would be characterized by a source moving roughly with half the beam velocity β_{NN}. This is at variance with the results listed above unless pion reabsorption considerably affects the primary distribution, and proves to be more important in the forward direction than at 90°. This assumption gains more in credibility when the rapidity distributions and the invariant cross sections are considered.

4.4 *Rapidity Distributions & Invariant Cross Sections.*

In Figure 24a, the laboratory rapidity distributions of pions produced in the three reactions studied here are shown. They are approximately gaussian in shape and have a Full Width at Half Maximum equal to 1.2 units of rapidity in each case. The centroid of the laboratory $d\sigma/dy$, indicated by an arrow on the rapidity axis, is equal to 0.07, 0.12 and 0.17 for ^{208}Pb, ^{58}Ni and ^{27}Al respectively. The centroid of the laboratory rapidity distribution provides another estimate of the average pion source velocity β_y for each colliding system.

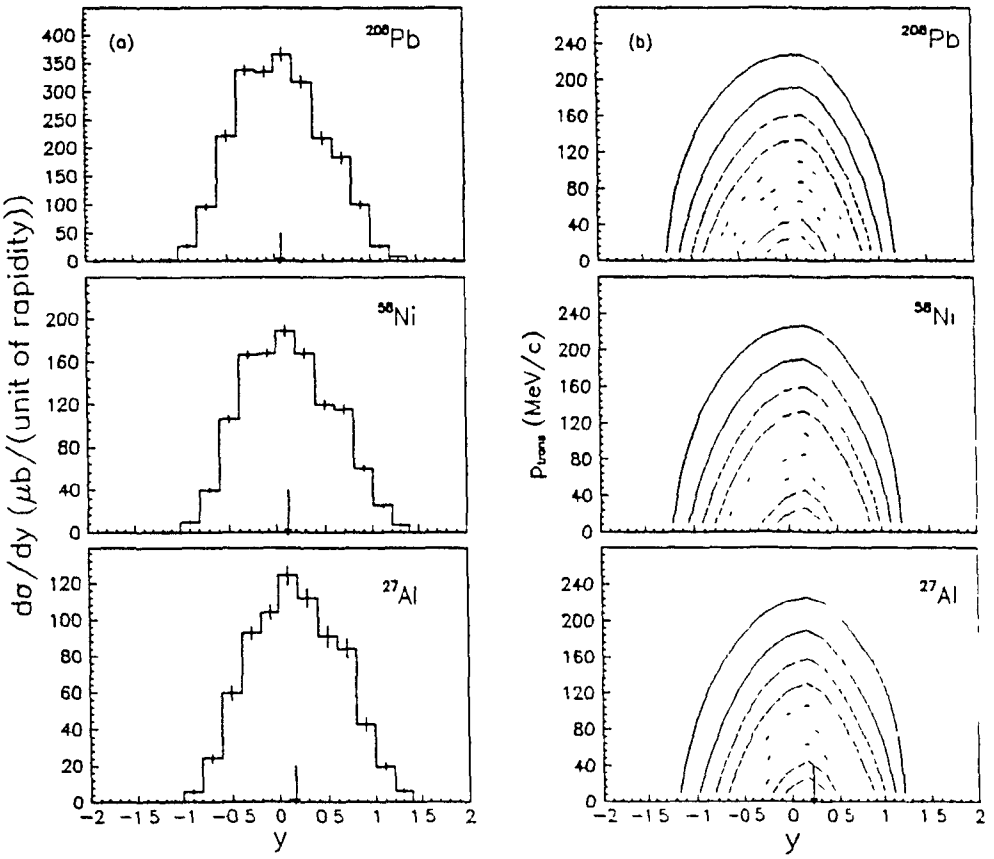

Fig. 24 (a) Laboratory rapidity distributions of pions produced in the reactions $^{16}O+^{27}Al$, ^{58}Ni, $^{208}Pb \rightarrow \pi^0+X$ at 95 MeV/u. The arrows correspond to the average source velocities. (b) Invariant cross sections for the same reactions. The arrow corresponds to the nucleon-nucleon rapidity y_{NN}=0.22.

Referring to Table 4.3, these are consistent with sources moving faster than the nucleus-nucleus center of mass but slower than the nucleon-nucleon system, which is in accordance with the velocities extracted from the angular distributions. The fact that β_y is lower than $\beta_{0\text{-}30}$ arises from the backward asymmetry of $d\sigma/dy$ with respect to its centroid.

The Lorentz invariant cross sections (3.12) are presented in Figure 24b for all three targets as contour plots in the transverse momentum versus rapidity plane. A B-spline smoothing has been applied to the raw data in order to obtain those plots. The cross section decreases by roughly a factor of 2 between two successive lines. In this representation, the invariant cross section is characterized by a family of successive ellipses. For all of the targets, σ_{inv} is centered on a rapidity value slightly lower than the nucleon-nucleon velocity indicated by the arrow. The invariant cross sections are clearly asymmetric about this central value. In fact, they show an excess of pions for lower rapidities. Moreover, the backward enhancement of the cross section is more important for the heavier targets. The asymmetry of σ_{inv} about the central rapidity value is a key feature of the present data. As will be discussed in the next chapter, this effect can be explained by a dominance of pion absorption in the forward direction. Such hypothesis would also explain the behavior of the source velocities obtained from the angular distributions. This will be further discussed in the next chapter, where the angular dependence of pion absorption is studied on the basis of the present results.

CHAPTER 5

DISCUSSION

5.1 The Thermal Source Model.

Pion production data at 95 MeV/u can be first examined to determine to which extent they are consistent with emission by a single thermal source [Ha65]. For pions, the available phase space in a perfectly thermalized volume follows the rules of Bose-Einstein statistics. One can therefore write:

$$\frac{d^3N}{d^3\vec{p}} = \frac{1}{\exp(E_\pi/T) - 1} \qquad (5.1)$$

where E_π is the total energy of the pions and T the temperature of the volume as it is defined in thermodynamics. In this formulation, the invariant production cross section is simply expressed as:

$$\sigma_{inv} = E_\pi \frac{d^3\sigma}{d^3\vec{p}} = C^{te} \frac{E_\pi}{\exp(E_\pi/T) - 1} \qquad (5.2)$$

where the constant is related to the formation cross section of the thermalized zone. The above expression can be compared to the experimental pion distribution in order to assess the validity of the thermal source picture for the reactions studied here. The natural first step is to derive the Lorentz invariant transverse momentum distribution. Since it is not affected by the source motion along the beam axis, $d\sigma/dp_t$ will depend only on the source temperature T and thus allow for its unbiased evaluation. One easily obtains the thermal source prediction for the transverse momentum distribution by numerical integration of the invariant cross section (5.2).

$$\frac{d\sigma}{dp_t} = K \int dy \, \frac{2\pi p_t E_\pi}{\exp(E_\pi/T) - 1} \qquad (5.3)$$

The agreement of equation (5.3) with the experimental transverse momentum distributions is shown in Figure 25. The constant K has been adjusted for each target to yield the integrated cross section. The spectral shape of $d\sigma/dp_t$ is very well reproduced by the thermal model. The best fit occurs for temperatures of 19±1 MeV, 20±1 MeV and 21±1 MeV for ^{208}Pb, ^{58}Ni and ^{27}Al respectively. The sensitivity to the temperature T is also shown in the case of ^{27}Al, for which the transverse momentum distributions calculated using T=19, 20 and 21 MeV are presented.

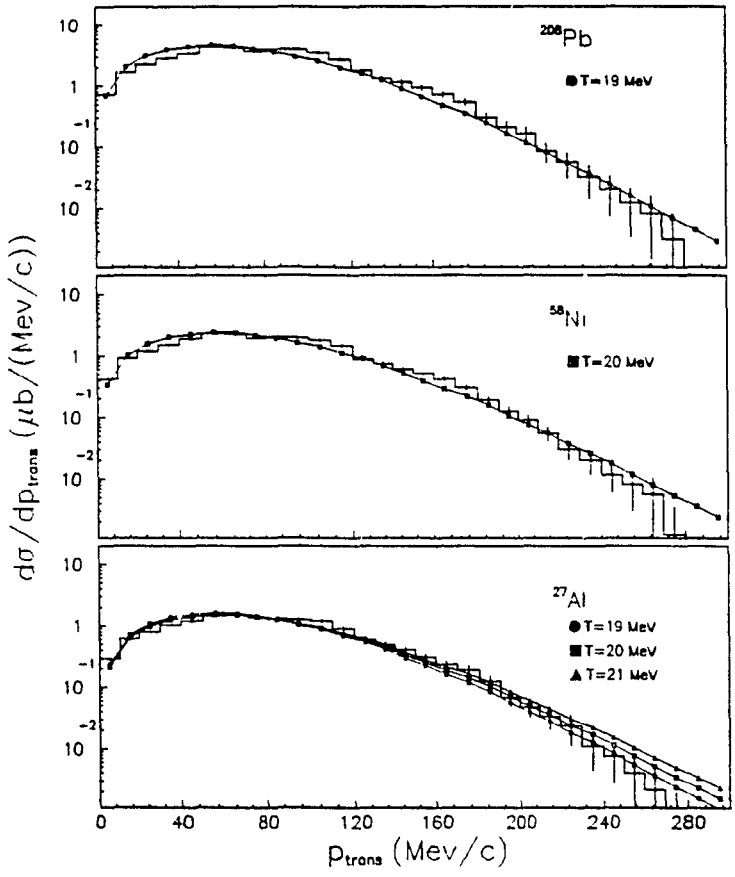

Fig. 25 Experimental transverse momentum distributions and the predictions of the thermal source model.

The source's temperature is nearly independent of the target mass, in agreement with the previous findings for the inverse slope parameters of the sideward kinetic energy distributions. This is an argument against pions being predominantly emitted by a compound nucleus involving all target and projectile nucleons. In such a mechanism, the available energy is shared by an increasing number of nucleons as the system's mass increases. This would cause a steep drop of the temperature for heavier targets at variance with the experimental observations.

A more likely situation involves the formation of a pion source from a subset of participant nucleons. Using conservation of momentum, one easily evaluates the number of target nucleons interacting with the projectile. For instance, a hot volume formed by the entire projectile and N_t participant target nucleons, would have the following center of mass velocity:

$$\beta_s = \frac{\gamma_p \beta_p A_p}{\gamma_p A_p + N_t} \qquad (5.4)$$

where β_p is the beam velocity and $\gamma_p=(1-\beta_p{}^2)^{-1/2}$. For the present reactions, taking β_S equal to the average pion source velocity $\beta_{0\text{-}30}$, one obtains that 57, 31 and 23 target nucleons would be embodied in the hot zone for ^{208}Pb, ^{58}Ni and ^{27}Al respectively. These figures are in perfect agreement with the fireball geometric prediction for the number of nucleons taken away by a zero impact parameter beam drilling a hole into the target [Go77, We76]. The assumption that pions originate from a thermalized moving source described by the fireball formalism is further suggested when the present data are compared to light particle measurements at similar beam energies. Figure 26 shows the systematics of moving source parameters extracted from ^{16}O-, ^{20}Ne-, ^{40}Ar- and ^{12}C-induced reactions on heavy nuclei [We82, Ha85].

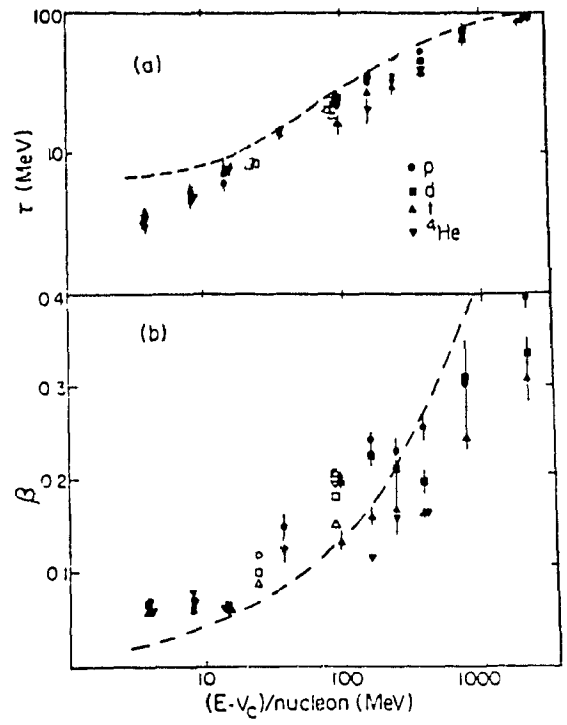

Fig. 26 Systematics of moving source parameters extracted from light particle spectra measured in O-, Ne-, Ar- and C-induced reactions [We82, Ha85]. (a) The extracted temperatures from the moving source compared with the fireball description (dashed line) [Go77]. (b) The moving source velocities compared with the fireball model. The figure is borrowed form the reference [Ha85].

The p, d, t and ^{4}He spectra measured at $E_{lab}/A \cong 100$ MeV/u have average temperatures of 23±3 MeV. Moreover, these temperatures are nearly independent of the colliding system. This is in agreement with the behavior of the temperatures observed for the present pion results. The apparent source velocities obtained for the pions also compare very well with those extracted from light particle data, which are grouped between $\beta_{SO}=0.10$ and $\beta_{SO}=0.20$. This similarity between pion and light particle production results, suggests that the former might predominantly originate from a hot zone described by the fireball geometry The success of this model in reproducing the experimental source parameters of light particles is displayed on Figure 26 by the dashed lines which agree with both the experimental temperatures and velocities over a large range of beam energies.

The angular evolution of the pion kinetic energy spectra can be used to test the thermal source assumption. The invariant cross section as written in equation (5.2) can be calculated for specific source velocities and temperatures and the angle integrated results compared with the experimental energy distributions. In Figure 27, the pion kinetic energy spectra measured for ^{208}Pb are set against the

predictions of equation (5.2). Using a temperature of 19 MeV, $d\sigma/dT_\pi$ has been calculated for sources moving respectively with. the nucleus-nucleus center of mass velocity β_{CM}=0 03, the average source velocity $\beta_{0\text{-}30}$=0.10, and the nucleon-nucleon velocity β_{NN}=0 22 The angle integrated spectrum is presented along with its projections in the forward $0^o \le \Theta_\pi \le 30^o$, sideward $60^o \le \Theta_\pi \le 120^o$ and backward $150^o \le \Theta_\pi \le 180^o$ directions. The calculated curves are normalized for each spectrum in order to yield the measured cross section in the energy range of 50 to 150 MeV. This emphasizes the behavior of the inverse slope parameter as the source velocity is changed and also overcomes the dependence of the production cross section upon the pion emission angle

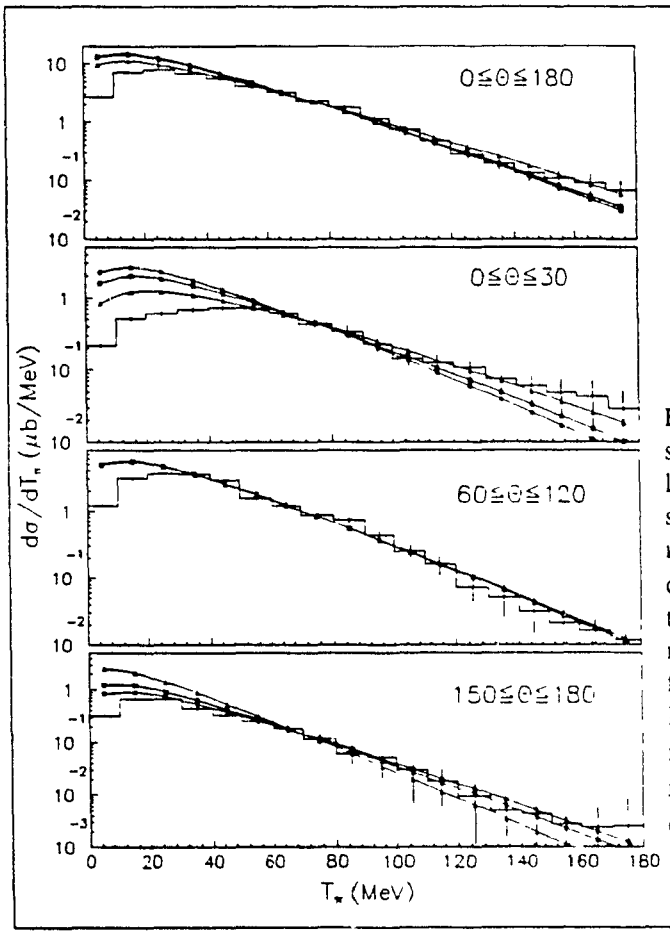

Fig. 27 Total, forward, sideward and backward laboratory kinetic energy spectra of pions produced in $^{16}O+^{208}Pb \rightarrow \pi^0+X$ as compared to predictions of the moving thermal source model The calculations are for a temperature of 19 MeV The source velocity β_{SO} is: full triangles $\beta_{SO}=\beta_{NN}$, full squares $\beta_{SO}=\beta_{0\text{-}30}$, full circles $\beta_{SO}=\beta_{CM}$

The naive thermal source model reproduces very well the experimental slopes in the sideward region regardless of the source velocity. This confirms that, for pions emitted at 90°, the inverse slope parameter is independent of the source kinematics as previously noted in Table 4 2. In this angular region, the slope of $d\sigma/dT_\pi$ is therefore

only determined by the thermal properties of the pion production source.

In Table 5.1, the experimental inverse slope parameters E_{0exp} that were obtained in the laboratory are compared to those resulting from moving sources of velocities β_{CM}, $\beta_{SO}=\beta_{0\text{-}30}$ and β_{NN} with respective temperatures of T=19, 20, 21 MeV for ^{208}Pb, ^{58}Ni and ^{27}Al.

Table 5.1: *Comparison of the experimental E_0 with predictions of the thermal source model.*

^{208}Pb

emis angle	*$E_{0\ exp}$(MeV)*	*$E_{0\ CM}$(MeV)*	*$E_{0\ SO}$(MeV)*	*$E_{0\ NN}$ (MeV)*
$0^o\le\Theta_\pi\le180^o$	26.9±0.9	25.4	26.2	29.5
$0^o\le\Theta_\pi\le30^o$	35.0±2.6	26.6	29.4	36.0
$60^o\le\Theta_\pi\le120^o$	25.1±1.3	25.3	25.4	25.8
$150^o\le\Theta_\pi\le180^o$	21.5±2.0	24.1	21.9	18.3
source velocity		β_{CM}=0.03	β_{SO}=0.10	β_{NN}=0.22
source temperature		T=19 MeV	T=19 MeV	T=19 MeV

^{58}Ni

emis angle.	*$E_{0\ exp}$(MeV)*	*$E_{0\ CM}$(MeV)*	*$E_{0\ SO}$(MeV)*	*$E_{0\ NN}$ (MeV)*
$0^o\le\Theta_\pi\le180^o$	29.8±0 8	27.8	29.1	31.3
$0^o\le\Theta_\pi\le30^o$	44.9±2.8	31.4	34.3	38.5
$60^o\le\Theta_\pi\le120^o$	25.7±1.0	27.1	27.2	27.4
$150^o\le\Theta_\pi\le180^o$	17.3±0.9	23.3	21.6	19.5
source velocity		β_{CM}=0.10	β_{SO}=0.15	β_{NN}=0.22
source temperature		T=20 MeV	T=20 MeV	T=20 MeV

^{27}Al

emis angle	*$E_{0\ exp}$(MeV)*	*$E_{0\ CM}$(MeV)*	*$E_{0\ SO}$(MeV)*	*$E_{0\ NN}$ (MeV)*
$0^o\le\Theta_\pi\le180^o$	32.9±1.5	31.2	31.6	33.2
$0^o\le\Theta_\pi\le30^o$	56.8±6.7	37.4	38.2	41.1
$60^o\le\Theta_\pi\le120^o$	25.0±1.6	29.0	29.0	29.2
$150^o\le\Theta_\pi\le180^o$	17.6±1.8	22.5	22.1	20.8
source velocity		β_{CM}=0.17	β_{SO}=0.18	β_{NN}=0.22
source temperature		T=21 MeV	T=21 MeV	T=21 MeV

As expected, if one only looks at the inverse slope of the total kinetic energy distributions ($0^o \leq \Theta_\pi \leq 180^o$), the experimental values are well reproduced for all three targets by a source of average velocity $\beta_{SO} = \beta_{0\text{-}30}$. However, regardless of the assumed velocity, the single thermal source model fails to reproduce the inverse slopes obtained in the forward, sideward and backward regions. In addition, for ^{58}Ni and ^{27}Al, the experimental E_0's found at forward angles are still considerably higher than what would be expected of a source at rest in the nucleon-nucleon center of mass frame. Ungated fast neutrons seen by the telescopes #4 & #5 could be the main source of this discrepancy. A few photon-neutron coincidences of reconstructed invariant mass close to $m_\pi c^2$ would be sufficient to considerably affect the temperature in the forward region.

For asymmetric colliding systems, emission from a single moving source is in fact very unlikely. The large cross sectional area offered by the target allows for the formation of several sources corresponding to different impact parameters [Pr86]. This picture is compatible with the observed kinetic energy distributions, and the only remaining features of the present data at our disposal to assess the full validity of the thermal prescription are the experimental angular distributions. The curves shown in Figure 28 are angular distributions calculated in the ^{27}Al's nucleus-nucleus center of mass according to the isotropic thermal source model (5.2), using a temperature T=21 MeV. Five velocities have been considered. The label β_T refers to a source at rest in the laboratory and is representative of a target-like contribution, on the other hand, β_P is associated with a source having the projectile's velocity. The curve labeled β_{CM} represents the emission of a thermal source at rest in the nucleus-nucleus center of mass and is isotropic in that frame, since equation (5.2) is independent of Θ_π. Finally, the curves labeled $\beta_{0\text{-}30}$ and β_{NN} correspond to pion emission from the average source and the nucleon-nucleon rest frames. All of these curves are normalized to the integrated cross section.

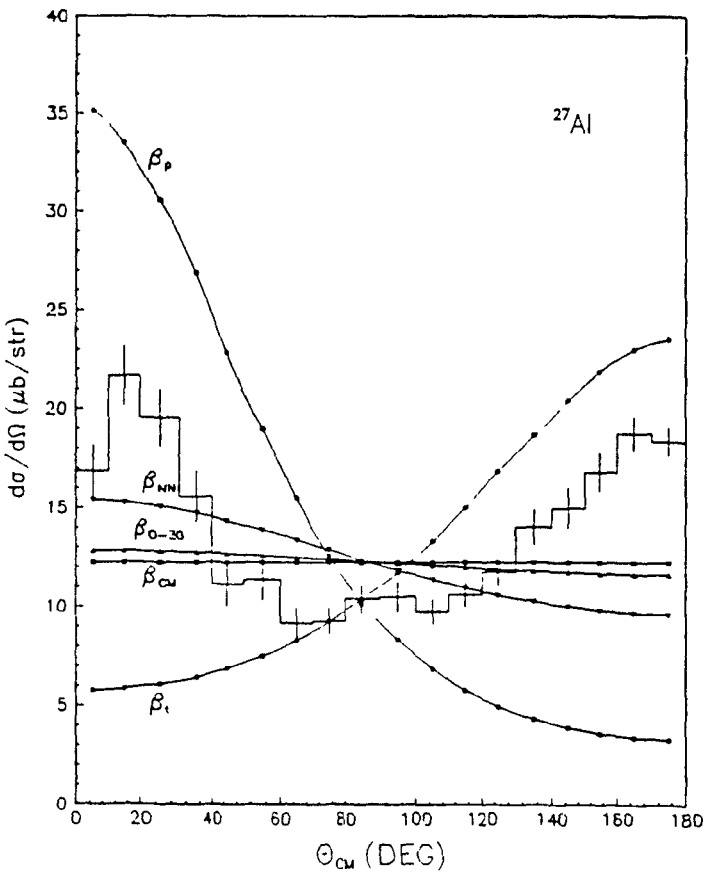

Fig. 28 Center of mass angular distribution of pions produced in $^{16}O+^{27}Al \rightarrow \pi^0+X$. The results are compared to predictions of the moving thermal source model. The calculations were performed for a temperature of 21 MeV. The various source velocities are indicated in each case.

The experimental angular distribution is clearly inconsistent with isotropic emission from a single thermal source. As is displayed above, such a source simply cannot give rise to the observed forward and backward enhancements of $d\sigma/d\Omega$. It is especially interesting to note that even a source moving with the nucleon-nucleon center of mass still underpredicts substantially $d\sigma/d\Omega$ at forward angles. Even assuming the presence of several thermal sources, with a given velocity and temperature distribution, the anisotropy of the angular distribution is unlikely to be reproduced by the thermal model. As shown on Figure 28, such a picture would be consistent with the shape of $d\sigma/d\Omega$ only if temperatures much higher than 21 MeV or if strong projectile and target-like components were involved in the production mechanism. The fireball model is certainly at variance with the data on this point. In this case, the projectile and target spectator fragments would be left

with an excitation energy insufficient to reach a thermalization of 20 MeV and produce pions.

The anisotropy of the angular distribution is the principal indication that thermal radiation, even if present, is not sufficient alone to account for all characteristics of subthreshold pion production at 95 MeV/u. A successful theoretical description of the pion results needs to include an anisotropic component in the primary distribution. For example, first chance $NN \rightarrow NN\pi$ collisions in the early stage of the reaction might contribute significantly to the pion yield at these energies and would introduce an intrinsic anisotropy in the angular distribution [Er88].

The anisotropy A_0, is a measure of the angle dependent part of $d\sigma/d\Omega$. In analogy to reference [Na81], it has been evaluated using:

$$A_0 = 0.5 \frac{\frac{d\sigma}{d\Omega}(\Theta_\pi = 15^0) + \frac{d\sigma}{d\Omega}(\Theta_\pi = 165^0)}{\frac{d\sigma}{d\Omega}(\Theta_\pi = 90^0)} \qquad (5.5)$$

According to (5.5), an isotropic angular distribution leads to $A_0 = 1$. The anisotropies obtained in the inertial frame moving with the average source velocity $\beta_{0\text{-}30}$ are listed in Table 5.2. For each target, this special inertial frame is such that the angular distribution is forward-backward symmetric.

Table 5.2: *Experimental anisotropies*

Target	*pion energy*	$A_0[\pm 0.2]$
^{208}Pb	$0 \le T_\pi \le 180$	1.7
	$5 \le T_\pi \le 30$	1.6
	$30 \le T_\pi \le 55$	1.7
	$55 \le T_\pi \le 125$	1.8
^{58}Ni	$0 \le T_\pi \le 180$	1.9
	$5 \le T_\pi \le 30$	1.6
	$30 \le T_\pi \le 55$	1.8
	$55 \le T_\pi \le 125$	2.1
^{27}Al	$0 \le T_\pi \le 180$	2.0
	$5 \le T_\pi \le 30$	1.7
	$30 \le T_\pi \le 55$	1.6
	$55 \le T_\pi \le 125$	2.6

The anisotropy increases with the pion kinetic energy in agreement with the results obtained at 84 MeV/u [No84]. On average, A_0 also decreases for heavier targets The same behavior is observed for A_0 in the nucleus-nucleus center of mass frame, although the values obtained in the highest energy range are affected by the source kinematics The anisotropic component present in the pion yield at 95 MeV/u is similar to that observed in reactions well above the $NN \rightarrow NN\pi$ threshold For instance, an anisotropy of roughly $A_0=2.5$ has been measured for low energy negative pions ($T_{\pi CM} \cong 100$ MeV) produced in 800 MeV/u Ar+KCl [Na81] Comparable values were also obtained in the same reaction at 1.8 GeV/u [Br84b]. On the other hand, much larger anisotropies result from single nucleon scattering processes $NN \rightarrow N\Delta \rightarrow NN\pi$. Values of A_0 greater than 3 were reported for positive pions of center of mass energy above 100 MeV produced in the reaction $pp \rightarrow \pi^+ d$ [Ri70].

The anisotropy of the angular distributions, is a key element in understanding subthreshold pion measurements It was shown that unless hot spectator-like components are present, the thermal source assumption leads to angular distributions which are nearly isotropic. In contrast, pions arising from single nucleon-nucleon collisions alone are experimentally characterized by anisotropies higher than those observed in heavy ion induced reactions One could try to explain the anisotropy of subthreshold pion measurements with some other assumptions For instance, the firestreak model [My78], which is a modified version of the fireball assumption where the reaction dynamics is parametrized by participant streaks of nucleons having different velocities and temperatures, could be considered Such a model would predict some anisotropy in $d\sigma/d\Omega$ arising from the source velocity distribution. Furthermore, this anisotropy would increase with the pion kinetic energy The reabsorption of pions in the surrounding matter after emission could also play a determinant role For example, collision dynamics in which the sideward pions have a higher probability to interact with the remnants of the reaction, could transform an initially isotropic emission into an anisotropic one. In contrast, maximum absorption in the forward direction would reduce the intrinsic anisotropy of single nucleon-nucleon collisions.

5.2 *Pion Reabsorption.*

As a consequence of reabsorption in the surrounding matter, the measured invariant cross section is a disturbed image of the primary pion emission. The large range of target masses, as well as the beam energy which has provided good statistics, allow for the isolation of relevant signatures of reabsorption in the pion distribution These signatures are discussed in the following paragraphs using the measured energy and angular distributions

The survival probability of pions after emission will, in first order, be determined by the quantity of matter traversed and the kinetic energy dependence of the mean free path Considering undeflected trajectories, one can approximate the probability that pions will live long enough to be observed by the following expression [Le87]:

$$p(A,T_\pi,\Theta_\pi) = \exp\left[- \frac{R_0 A^{1/3}\, x(\Theta_\pi)}{\lambda(T_\pi)} \right] \qquad (5.6)$$

In (5.6), the kinetic energy dependence of pion absorption is expressed explicitly by the mean free path $\lambda(T_\pi)$ The quantity of matter traversed for a given pion emission angle Θ_π, is assumed to depend on the target radius, $R_0 A^{1/3}$, since one expects the absorption to increase with the target mass. The average location of the pion source in the system formed by the interacting nuclei is unknown, and one must therefore consider the influence of the collision geometry on the angular dependence of the absorption. This dependence is expressed here as the function $x(\Theta_\pi)$. For example, if the source is a hot spot located at the center of a compound system, then $x(\Theta_\pi)$ will be a constant and the absorption will depend on the radius only On the other hand, if full stopping occurs in the collision before the projectile reaches the target's center, $x(\Theta_\pi)$ will be at its maximum in the forward direction, and so will the absorption.

In the source rest frame, the observed invariant cross section for a given target results from folding the primary production cross section by the survival probability (5.6) as follows:

$$\sigma_{inv}^{exp} = p(A,T_\pi,\Theta_\pi)\,\sigma_{inv}^{prim} \qquad (5.7)$$

Our aim is to extract from the data some information about the dependence of pion absorption in both, the kinetic energy, and the emission angle. This can be done if the assumption is made that the primary invariant cross sections involved in the three reactions studied here are all alike, and only differ in first approximation by a scaling factor related to the target mass This assumption is justified by two experimental observations: firstly, in the thermal moving source picture, the transverse momentum distributions lead, within the uncertainty, to a unique temperature of 20 MeV; secondly, the anisotropy A_0 of low kinetic energy pions, which form the bulk of the statistics, depends only weakly upon the target mass [see Table 5 2]. This indicates that the physics involved in subthreshold pion production at this beam energy does not change drastically with the target. It is therefore reasonable to consider the absorption as being responsible for the observed differences in the distributions from one target to another Of course, any signature based on this assumption will be valid only if the two following conditions are met. First, the dependence of the absorption on the kinetic energy and emission angle must increase with the target mass Second, these two dependences should be relatively insensitive to the source dynamics, i.e. the absorption signatures must be unaffected by the source velocities.

If the primary invariant cross sections are assumed to be similar, except for a constant which is determined by the target mass, then the ratios of kinetic energy and angular distributions measured for different targets should be dominated by the absorption effects. In the limit of small absorption, using $d\sigma/dT_\pi$ as obtained in the respective source rest frame, the pion survival probability's dependence upon its kinetic energy is approximately given by the empirical rule:

$$P(T_\pi,A_1,A_2) = \frac{\left[\frac{1}{\sigma}\frac{d\sigma}{dT_\pi}\right]_{A_1,\,\beta_1}}{\left[\frac{1}{\sigma}\frac{d\sigma}{dT_\pi}\right]_{A_2,\,\beta_2}} \qquad (5.8)$$

while the angular dependence should be given by:

$$P(\Theta_\pi, A_1, A_2) = \frac{\left[\frac{1}{\sigma}\frac{d\sigma}{d\Omega}\right]_{A_1, \beta_1}}{\left[\frac{1}{\sigma}\frac{d\sigma}{d\Omega}\right]_{A_2, \beta_2}} \qquad (5.9)$$

where, by definition, the target mass A_1 is larger than A_2. Each distribution is normalized to its integrated cross section σ in order to keep (5.8) and (5.9) close to one. Because they are survival probabilities $P(T_\pi, A_1, A_2)$ and $P(\Theta_\pi, A_1, A_2)$ as defined will be minimal when the absorption is strong, and close to one if reabsorption effects are not important for given T_π or Θ_π. In absence of any other assumptions on the scale of the primary invariant cross section of each target, the equations above do not provide the absolute value of the absorption. Only the dependence of the absorption probability upon the kinetic energy and the emission angle can be approximately determined.

5.2.1 *Kinetic Energy Dependence.*

As was pointed out above, in order to isolate the absorption probability, one must compare the pionic emission from different targets in their respective average source rest frame, since otherwise the conclusion would be affected by kinematical effects. For the energy dependence of the absorption, this problem can be overcome by comparing the kinetic energy distributions of pions emitted in the sideward region, $60^{o} \leq \Theta_{\pi} \leq 120^{o}$, which proved to be independent of the observation frame. Results of equation (5.8) are shown for sideward pions in Figure 29, where all three possible target pairs are presented.

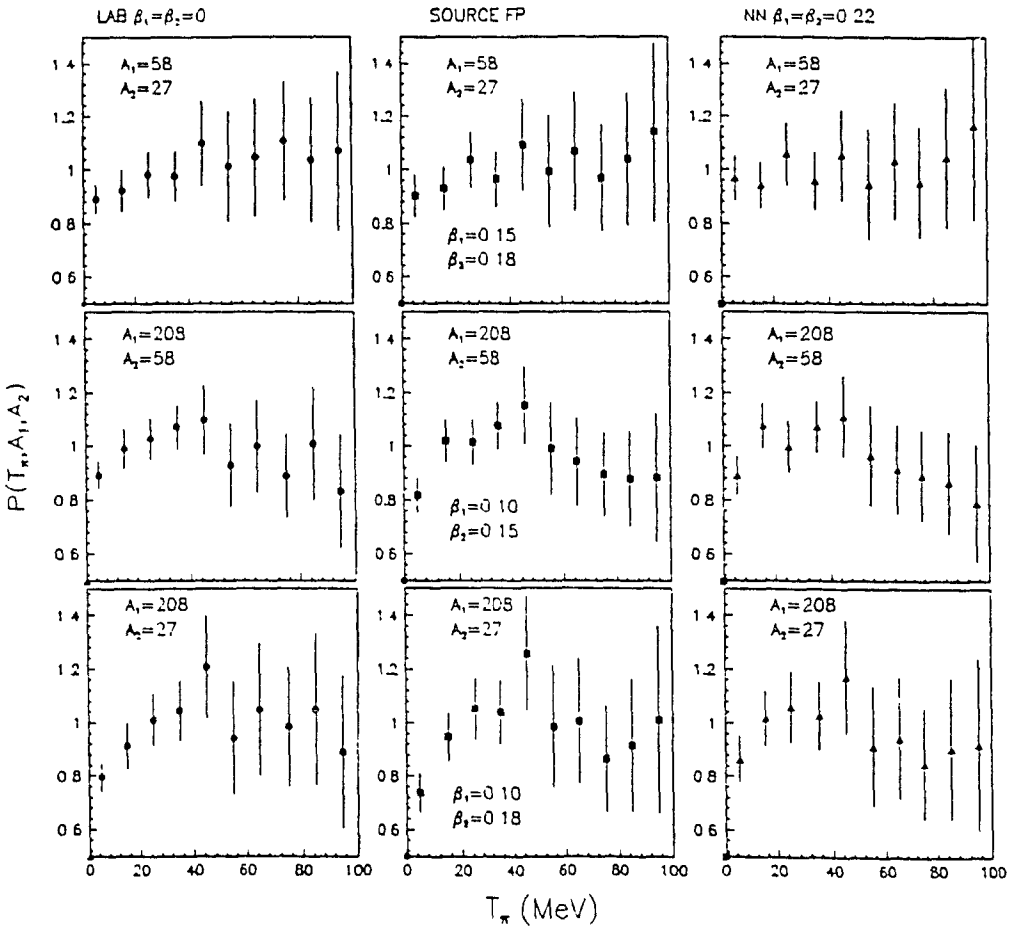

Fig. 29 Kinetic energy dependence of pion absorption as deduced from equation (5.8) using sideward pions only. The kinetic energy distributions of targets A_1 and A_2 are compared in the laboratory (left), the respective source rest frames (center), and the nucleon-nucleon system (right).

To display the insensitivity of the results upon the kinematics, the ratio (5.8) was calculated using for each target, $d\sigma/dT_\pi$ as obtained in: the laboratory, the respective source rest frame and the nucleon-nucleon center of mass. In addition, it was verified that the trend is unaffected if all pion emission angles are considered. The dependence of the absorption effects upon the growing target mass difference is clearly visible. For the case of $A_1=^{58}Ni$ & $A_2=^{27}Al$, because of the small mass difference between these two targets, $P(T_\pi, A_1, A_2)$ is rather constant with a value close to 1 except for low kinetic energy pions As the mass difference increases, the survival probability (5.8) deviates from 1 and indicates a large absorption for low kinetic energy pions Moving toward higher energies, one observes a minimum absorption for pions of $T_\pi \cong 40$ MeV followed by a new rise of reabsorption effects above 50 MeV.

The large absorption for pions of low kinetic energy is also apparent on Figure 30.

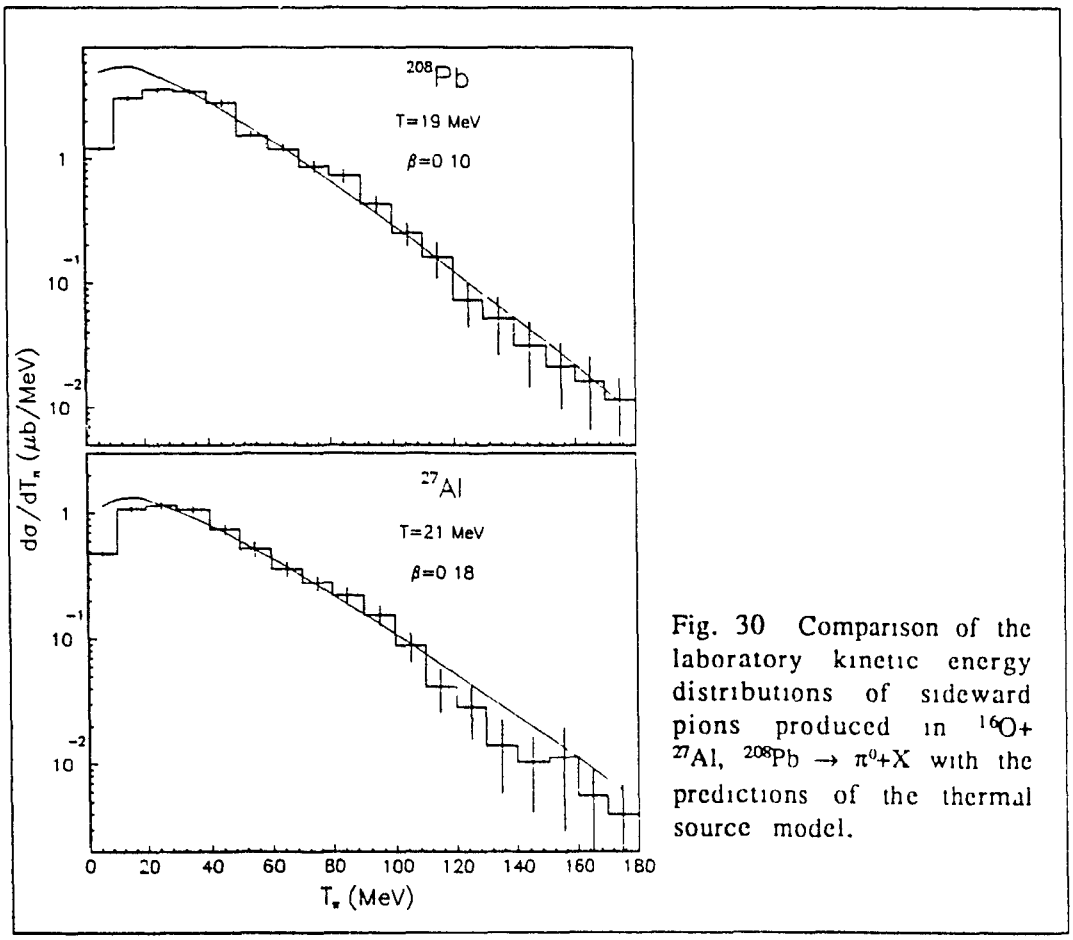

Fig. 30 Comparison of the laboratory kinetic energy distributions of sideward pions produced in $^{16}O+^{27}Al$, $^{208}Pb \rightarrow \pi^0+X$ with the predictions of the thermal source model.

This figure presents the laboratory kinetic energy distributions of sideward pions obtained for ^{208}Pb and ^{27}Al along with predictions of the thermal source model (5.2). The experimental distributions show a lack of pions below T_π=40 MeV when compared to the calculated spectra. As expected, this effect is much more important for the heaviest target ^{208}Pb.

Pion absorption cross sections are available in the literature but only for kinetic energies higher than 37 MeV and for nuclei in their ground state [As80, Na80, Na83]. These are inappropriate for our discussion, since the better part of the pions observed in the present experiment have an energy lower than 37 MeV. Moreover, the reabsorption is due to excited remnants created during the reaction. Hufner and Thies [Hu79] have calculated low energy pions absorption using a transport calculation method to follow the pions in normal density nuclear matter. In their model the pion-nucleus optical potential and the elementary pion-nucleon cross section are used as dynamical input. They reproduce to a satisfactory level the existing pion absorption cross sections above 37 MeV. An optical model calculation is relevant here, since it reflects the absorption at the surface of the nuclear matter where pions emitted in subthreshold production are most likely to be absorbed when they interact with the collision remnants. The mean free path $\lambda(T_\pi)$, deduced from this calculation [using an absorption width of Γ=120 MeV] is shown in Figure 31 along with the result of a similar relativistic calculation by Mehrem et al. [Me84].

The mean free path resulting from both calculations agrees with the overall trend of the survival probability $P(T_\pi, A_1, A_2)$ deduced from our data. They show a minimum absorption for pions of kinetic energy close to 40 MeV and stronger effects below and above that value. Note that according to these calculations, one would expect $\lambda(T_\pi)$ to be minimum for pions of kinetic energy above 75 MeV, while the trend of $P(T_\pi, A_1, A_2)$ agrees more with a minimum mean free path for pions having T_π lower than 20 MeV.

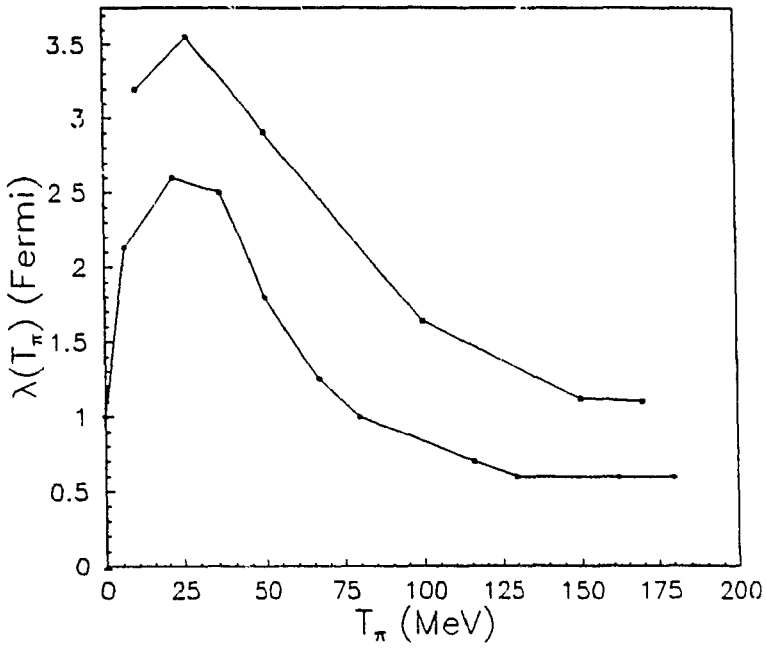

Fig. 31 Calculated mean free paths as a function of the pion energy; full squares: [Hu79], full circles: [Me84].

The theoretical $\lambda(T_\pi)$ is also very small, especially in the calculation of Mehrem et al. Assuming that the pions traverse a distance roughly equal to the target radius, a mean free path of $\cong 1.5$ fermi would lead to striking differences in the shape of the energy spectra obtained for ^{27}Al and ^{208}Pb respectively. This is at variance with our findings, since Figure 29 clearly indicates that reabsorption effects do not completely dominate the shape of the energy spectra but are rather perturbations affecting the primary distributions. It seems that the pions have a large effective mean free path. This could arise from the reaction geometry; for example, in the fireball prescription, by the time pions get emitted, the spectator fragments may already be too far from the participant zone to cause large absorption.

5.2.2 *Angular Dependence.*

The angular dependence of absorption is dominated by the geometrical configuration of the pion emission system created by the participant nucleons, and the location of this hot zone with respect to the spectator fragments. To enhance the trend of reabsorption as a function of the pion emission angle, the angular distributions of low kinetic energy pions, which are most affected by reabsorption, were studied. Figure 32 presents the results of equation (5.9) for all three target pairs. Only those pions having a kinetic energy in the range $5 \leq T_\pi \leq 30$ MeV have been considered. In order to cancel out the effect of the different source velocities, the angular distributions used to calculate $P(\Theta_\pi, A_1, A_2)$ are those obtained in the respective average source rest frame of each target.

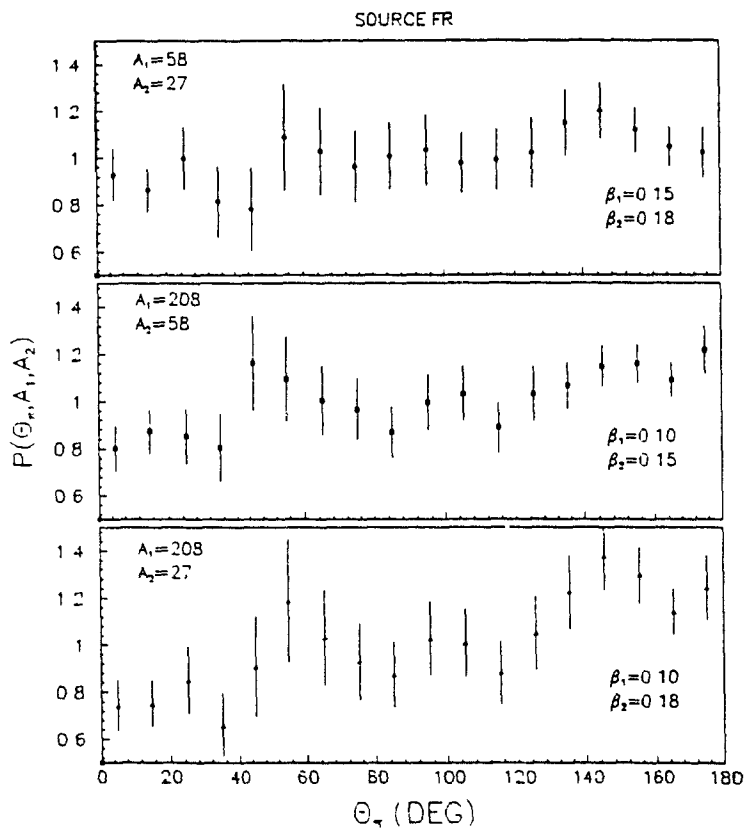

Fig. 32 Angular dependence of pion absorption as deduced from equation (5.9) using low energy pions only. The angular distributions of targets A_1 and A_2 are compared in their respective source rest frame.

On average, the value of $P(\Theta_\pi, A_1, A_2)$ increases with the pion emission angle. As expected, this effect is also more pronounced for larger target mass differences. These curves indicate that reabsorption is dominant in the forward direction. This trend does not change when all kinetic energies are considered, although the difference seen in $P(\Theta_\pi, A_1, A_2)$ between the forward and backward angles is smaller

A somewhat cleaner signature of forward absorption is present in the rapidity distribution. In Figure 33, the laboratory rapidity spectra of pions with small transverse momentum ($0 \le p_t \le 50$ MeV/c) are shown. The mean source rapidity corresponding to $\beta_{0\text{-}30}$ is indicated by an arrow for each target. This representation offers the advantage of being free of the kinematics, since p_t is Lorentz invariant and $d\sigma/dy$ only shifts by a constant along the rapidity axis under a velocity boost.

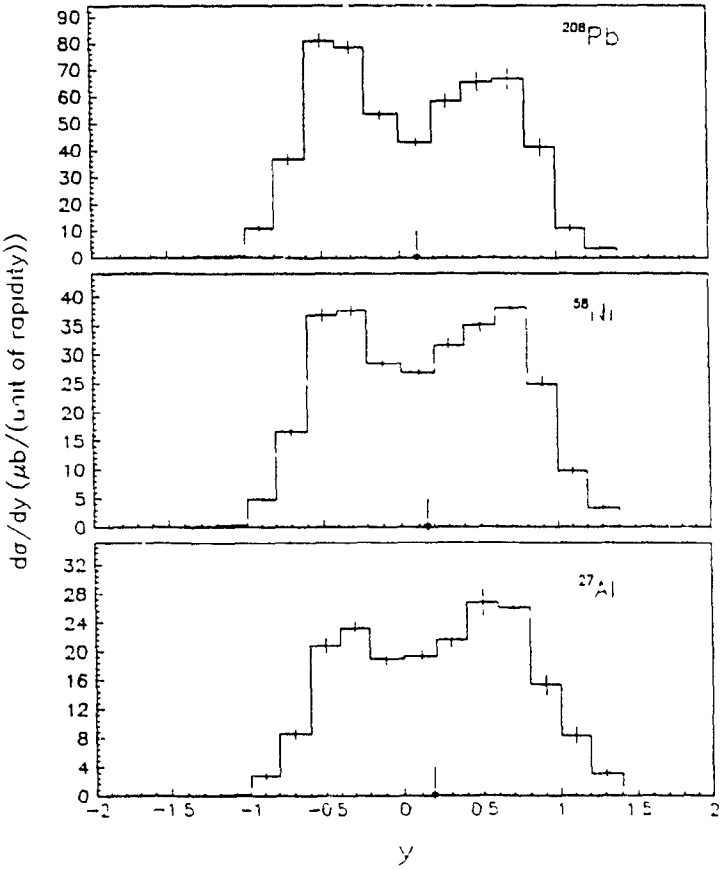

Fig. 33 Laboratory rapidity distributions of low transverse momentum pions ($0 \le p_t \le 55$ MeV/c). The average source rapidity corresponding to $\beta_{0\text{-}30}$ is indicated by an arrow for each target.

Pions with low transverse momentum are predominantly emitted in the forward or backward directions, since most of their energy is carried along the beam axis. However, in the absence of absorption, no preference should exist between these two directions even if the source has some anisotropy in its own rest frame. Clearly, when one compares the shape of $d\sigma/dy$ about the source rapidity, an excess of backward pions exists for ^{208}Pb, while, within the error bars, the distributions are symmetric for both the ^{58}Ni and ^{27}Al targets. This mass dependence of $d\sigma/dy$ agrees with stronger pion absorption in the forward direction.

5.2.3 Absorption and the Thermal Source Model.

The thermal source model provides the invariant cross section prior to the effect of pion absorption. The present data demonstrate that the consequence of this perturbation on the primary distribution is a net reduction of low energy pions in the forward direction. Therefore, one should not be surprised by deviations from this naive model. In this last section, the discrepancies between the experimental results and the thermal source model predictions are discussed in light of reabsorption effects. This approach should provide an improved understanding of the overall characteristics of the energy and angular distributions.

In Figure 34, the forward, sideward and backward laboratory kinetic energy distributions are compared for each target with predictions of the single thermal source model (5.2). The temperatures and velocities used for the calculations are indicated on the figure. The theoretical curves are normalized to the experimental cross section between 50 MeV and 150 MeV. For low energies, the perturbations introduced in $d\sigma/dT_\pi$ by pion reabsorption are quite apparent when the experimental spectra are set against the thermal source prescription at various emission angles. The forward spectra are characterized by a maximum cross section at energy values 30 to 40 MeV higher than the prediction of the thermal source model. The same shift, although less important is seen sideward. For backward emission, both the experimental and calculated maxima of $d\sigma/dT_\pi$ agree for all targets. Furthermore, at low energies, the ratio of the experimental and calculated cross sections shows an increasing lack of pions as one goes toward smaller emission angles. The amount of missing pions also increases with the target mass. These observations are in agreement with an enhancement of reabsorption for low kinetic energy pions emitted in the forward direction. The disappearance of a sizeable fraction of these π^0's after emission, would explain the large shift of the $d\sigma/dT_\pi$ maximum observed at forward angles for ^{208}Pb. Note that the greater average source velocity obtained for ^{27}Al as compared to ^{208}Pb should cause $d\sigma/dT_\pi$ to peak at higher laboratory energies for ^{27}Al than ^{208}Pb, in contrast to what is observed.

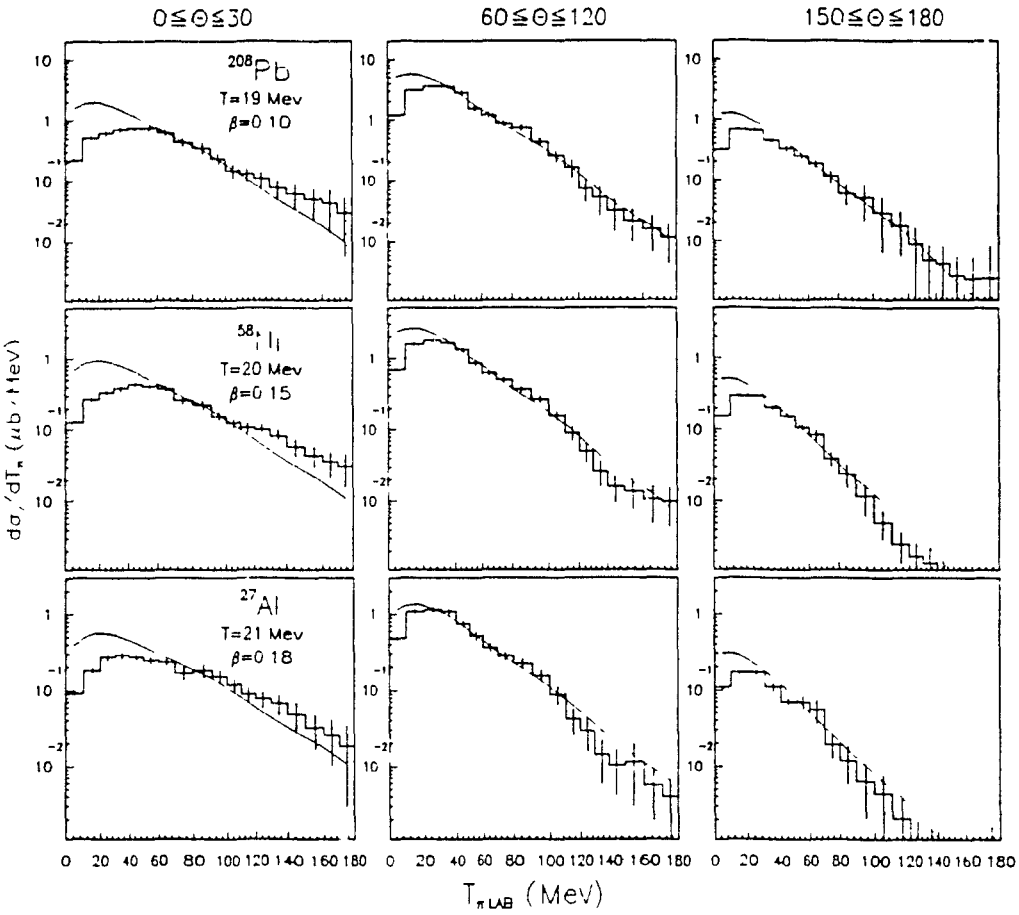

Fig. 34 Laboratory kinetic energy distributions of forward (left), sideward (center) and backward (right) pions as compared to the predictions of the thermal source model. The average source temperature and velocity used in the calculations are indicated for each target

The increased absorption above T_π=40 MeV should lead, for heavier targets, to a reduction of the apparent source's temperature in the forward direction. However, the forward spectra display the opposite behavior As was discussed in the previous section, this departure is probably due to the presence of a few background events and cannot be interpreted as a result of higher forward temperatures. The apparent lack of sideward and backward pions above 110 MeV in ^{58}Ni and ^{27}Al is not significant either. This effect is well within the ±1 MeV uncertainty on the temperature. In fact, from the survival probability curves shown in Figure 29 [Source frame], it can be shown that the effect of absorption on the primary temperature is small. In the case of A_1=^{208}Pb & A_2=^{58}Ni, the value of $P(T_\pi,A_1,A_2)$ decreases by 25% from T_π=40 MeV to T_π=100 MeV. Assuming this corresponds to a diminution of 25% of the primary kinetic energy distribution at T_π=100

MeV, it can be estimated, using equation (5.2), that a primary temperature of 21 MeV would be lowered to an apparent value of 19 MeV by such an attenuation. Such a small variation is at the limit of the sensitivity of our data to the temperature, it is therefore not surprising that no significant signature of absorption is found in the exponential part of $d\sigma/dT_\pi$.

An important consequence of pion reabsorption is that $\beta_{0\text{-}30}$ is in fact a lower estimate of the average source velocity This arises because it was deduced by equating the forward and backward emission probabilities. This evaluation method is obviously biased if the forward direction is preferentially attenuated. Therefore, solely considering the angular distributions, the only valid result for the source velocities is $\beta_{0\text{-}30} \leq \beta_{SO} \leq \beta_{NN}$. However, more can be said when the angular distributions obtained in the nucleon-nucleon center of mass are considered [see Figure 23]. For example, in this frame, one observes in $d\sigma/d\Omega$ a diminution of 55% from $\Theta_\pi=180^o$ to $\Theta_\pi=0^o$ for the ^{208}Pb target It is unlikely that such a strong backward asymmetry of the angular distribution would be due to reabsorption effects alone. In fact, the results presented in Figure 32 show that in the case of $A_1=^{208}Pb$ & $A_2=^{27}Al$, the value of $P(\Theta_\pi,A_1,A_2)$ decreases by only 35% from $\Theta_\pi=180^o$ to $\Theta_\pi=0^o$ This would indicate that the backward asymmetry of $d\sigma/d\Omega$ in the nucleon-nucleon rest frame does not only arise from forward absorption, but is also due to an effective primary source moving slower than β_{NN}.

The observed mass dependence of the angular anisotropy A_0 can also find an interpretation in terms of the absorption Stronger absorption in the forward direction can only lead to a reduction of the anisotropy in heavier targets This effect is observed on average in our angular distributions. Considering the lower kinetic energy range, ($5 \leq T_\pi \leq 30$ MeV), the anisotropy decreases steadily from ^{27}Al to ^{208}Pb. The values taken by A_0 in the slice $55 \leq T_\pi \leq 125$ MeV, which contributes most to the anisotropic component of $d\sigma/d\Omega$, also display this behavior In this case, one observes a much larger anisotropy for ^{27}Al than for ^{58}Ni and ^{208}Pb.

The experimental mass and energy dependences of the anisotropy also seriously contradicts an hypothesis which would state

that a maximum sideward absorption of isotropic pions is the cause of the dip in $d\sigma/d\Omega$ at 90^o. In such a picture, where the anisotropy is only related to the absorption, one would expect it to increase with the target mass. Furthermore, according to the observed energy dependence of the absorption, the anisotropy should be much higher for pions below 30 MeV than for any others The observed increase of A_0 for higher energies and smaller target masses, is impossible to reconcile with this assumption. The anisotropy observed for the ^{27}Al target, for which the effect of absorption is minimal, must then be considered as a lower limit on the anisotropic component present in the primary distribution at this beam energy. To what extent, the absorption, even in ^{27}Al, could explain that the measured anisotropies are much lower than those characteristic of single $NN \rightarrow NN\pi$ processes remains an open question.

CHAPTER 6

CONCLUSION

This study of subthreshold pion production at 95 MeV/u took advantage of the large statistics collected for a wide range of target masses. The analysis of the experimental results aimed firstly to isolate signatures helpful in understanding the mechanisms involved in subthreshold pion production, and secondly to discuss the influence of pion reabsorption effects on the important features of the data

The results were first analyzed in the framework of the moving thermal source model. This model reproduces very well the overall shape of the pion transverse momentum distributions obtained for ^{208}Pb, ^{58}Ni and ^{27}Al From these spectra, assuming the presence of a single source, it was deduced that the temperature of the pion emission system is close to 20 MeV. A symmetrization of the forward and backward emission probability has provided the apparent source velocity, which, for each colliding system, is between that of the nucleus-nucleus and nucleon-nucleon center of mass rest frames. The temperatures and velocities obtained for the present pion data also agree with those extracted from light particle spectra measured at similar beam energies. This first approach would therefore suggests that subthreshold pion production could be reproduced by a thermal model without any need for further assumptions

However, a closer inspection has shown that if the shape of the transverse momentum and angle integrated kinetic energy distributions are well described by a single moving thermal source, this model fails to reproduce the angular dependence of the inverse slope parameters obtained from the laboratory kinetic energy distributions Furthermore, even assuming several sources to contribute to the pion yield, the thermal model cannot account for the

anisotropy of the angular distributions unless hot projectile and target-like components are considered.

In attempt to explain the discrepancies between the thermal model and the present results, the effects of the reabsorption of the pions after their emission have been considered. An estimation of the energy and angular dependences of absorption was obtained from the experimental pion production cross sections by comparing the kinetic energy and angular distributions obtained for increasing target masses. The results of this approach show a dominance of absorption for pion of kinetic energy below 30 MeV. These results also agree in trend with optical model predictions. From the angular distributions it was concluded that absorption effects are dominant in the forward direction.

The influence of the reabsorption on some important features of the data have been discussed. For instance, a maximum absorption of low energy pions results in a significant shift of the maximum of the kinetic energy distributions which is observed when the data are compared to the predictions of the thermal source model. Also, a dominance of absorption for pions emitted forward implies a reduction of the anisotropy for increasing target masses, which is observed in the present data.

The deduced enhancement of absorption in the forward direction affects as well the picture of the production source. Such an angular dependence of reabsorption is consistent only if the pions originate from a source behind the target center and are more shadowed by the forward remnants of the reaction. Signatures of this shadowing were found in the asymmetry of the invariant cross sections and the mass dependence of the rapidity distributions for pions having a low transverse momentum. In addition, the apparent velocity of the pion source is reduced by forward absorption. As a consequence, the primary source could have a velocity much closer to that of the nucleon-nucleon system than what is deduced from the experimental angular distributions This could indicate that the pions are produced at a stage of the collision earlier than expected in the thermal source picture.

Of course the descriptive approach adopted here cannot replace a full dynamical model. However, it allowed to find the features of the results which are significant tests of a deeper theoretical study of the reaction mechanisms. For instance, the models should reproduce the angular dependence of the kinetic energy spectra and the anisotropy of the angular distributions. Much attention should also be paid to the dependence of these variables upon the mass of the colliding system.

Appendix

The Collaboration:

C. Moisan, J. Barrette, S.K. Mark
Foster Radiation Laboratory
McGill University

N. Alamanos, Y. Cassagnou, J.M. Hisslcur, J. Julien, R. Lacey,
R. Legrain, P. Roussel-Chomaz
CEN de Saclay

V. Bellini
INFN, Catania

G. Ingold, J. Stachel
SUNY, Stony Brook

REFERENCES

[Ai84a] J. Aichelin & G. Bertsch, Phys. Lett. **138B**, 350 (1984).

[Ai84b] J. Aichelin, Phys. Rev. Lett. **52**, 2340 (1984).

[Ai85] J. Aichelin, Phys. Lett. **164B**, 261 (1985).

[As80] D. Ashery, Nucl. Phys **A335**, 385 (1980).

[Ba81] H. W. Baer *et al*, Nucl. Instrum Methods **180**, 445 (1981).

[Be74] J. S. Beale *et al*, Nucl Instrum. Methods **117**, 501 (1974).

[Be77] G. F. Bertsch, Phys. Rev C **15**, 713 (1977).

[Bl85] M. Blann, Phys. Rev. C **32**, 1231 (1985).

[Br84a] P. Braun-Munzinger *et al.*, Phys. Rev. Lett. **52**, 255 (1984).

[Br84b] R. Brockmann *et al.*, Phys. Rev. Lett. **53**, 2012 (1984).

[Br87] P. Braun-Munzinger & J. Stachel, Ann. Rev. Nucl. Part. Sci. **37**, 97 (1987).

[Ca88] W. Cassing, Z. Phys. **A 329**, 487 (1988).

[Er88] T. Ericson & W. Weise, *Pions and Nuclei*, Clarendon Press, Oxford, 1988, Chapter 4, p. 101.

[Fa82] C. W. Fabjan & T. Ludlam, Ann. Rev. Nucl. Part. Sci. **32**, 335 (1982).

[Ga84] C. Gale & S. Das Gupta, Phys. Rev. C **30**, 414 (1984).

[Go77] J. Gosset *et al.*, Phys. Rev. **C 16**, 629 (1977).

[Gr85] E Grosse, Nucl. Phys. **A447**, 611c (1985).

[Gu84] C. Guet & M. Prakash, Nucl Phys **A428**, 119c (1984).

[Ha65] R. Hagedorn, Suppl. Nuovo Cimento **3**, 147 (1965).

[Ha85] B. E. Hasselquist *et al.*, Phys. Rev. C **32**, 145 (1985).

[He84] H. Heckwolf *et al*, Z. Phys. **A 315**, 243 (1984).

[Hu79] J. Hüfner & M. Thies, Phys. Rev. C **20**, 273 (1979).

[Ja75] J. D. Jackson, *Classical Electrodynamics* 2nd ed, John Wiley & Sons, New York, 1975, p. 638.

[Jo82] T. Johansson *et al*, Phys. Rev. Lett **48**, 732 (1982).

[Ju88a] J. Julien *et al.*, Z. Phys. **A 330**, 83 (1988).

[Ju88b] J. Julien *et al*, unpublished.

[Le87] W. R. Leo, *Techniques for Nuclear and Particle Physics Experiments*, Springer-Verlag, New York, 1987, p. 19.

[Mc47] W. G. McMillan & E. Teller, Phys. Rev. **72**, 1 (1947).

[Me84] R. A. Mehren, H. M. A. Radi & J. O. Rasmussen, Phys. Rev. C **30**, 301 (1984).

[Mi86] C. Michel *et al.*, Nucl. Instrum. Methods **A243**, 395 (1986).

[My78] W. D. Myers, Nucl. Phys. **A296**, 177 (1978).

[Na80] K. Nakai *et al*, Phys. Rev. Lett. **44**, 1446 (1980).

[Na81] S. Nagamiya *et al*, Phys. Rev. C **24**, 971 (1981).

[Na83] I. Navon *et al*, Phys. Rev. C **28**, 2548 (1983).

[No84] H. Noll *et al*, Phys. Rev. Lett. **52**, 1284 (1984).

[Pe87a] D. H. Perkins, *Introduction to High Energy Physics* 3rd ed., Addison Wesley, Menlo Park, California, 1987, p. 55.

[Pe87b] D. H Perkins, *Introduction to High Energy Physics* 3rd ed., Addison Wesley, Menlo Park, California, 1987, p. 139.

[Pr86] M. Prakash, P. Braun-Munzinger & J. Stachel, Phys. Rev. C **33**, 937 (1986).

[Ri70] C. Richard-Serre *et al*, Nucl. Phys. **B20**, 413 (1970).

[Se77] E. Segrè, *Nuclei and Particles* 2nd ed., Benjamin Cummings, Menlo Park, California, 1977, p. 911.

[Sh84a] R. Shyam & J. Knoll, Phys. Lett. **136B**, 221 (1984).

[Sh84b] R. Shyam & J. Knoll, Nucl. Phys **A426**, 606 (1984).

[Sh86] R. Shyam & J. Knoll, Nucl. Phys. **A459**, 732 (1986).

[St86] J. Stachel *et al*, Phys. Rev. C **33**, 1420 (1986).

[To84] M. Tohyama *et al*, Phys Lett. **136B**, 226 (1984).

[To85] M. Tohyama *et al*, Nucl. Phys. **A437**, 739 (1985).

[We76] G. D. Westfall *et al*, Phys. Rev. Lett. **37**, 1202 (1976).

[We82] G D. Westfall *et al*, Phys. Lett. **116B**, 118 (1982).

[Yo86] G. R Young *et al*, Phys. Rev. C **33**, 742 (1986).